Holographic entanglement renormalisation of topological order in a quantum liquid

Anirban Mukherjee[a] Siddhartha Lal,[a,1]

[a]*Department of Physical Sciences, Indian Institute of Science Education and Research Kolkata,India*

E-mail: am14rs016@iiserkol.ac.in, slal@iiserkol.ac.in

ABSTRACT: We introduce a novel momentum space entanglement renormalization group (MERG) scheme for the topologically ordered (T.O.) ground state of the 2D Hubbard model on a square lattice (arxiv:1802.06528) using a unitary quantum circuit comprised of non-local unitary gates. At each MERG step, the unitary quantum circuit disentangles a set of electronic states, thereby transforming the tensor network representation of the many-particle state. By representing the non-local unitary gate as a product of two-qubit disentangler gates, we provide an entanglement holographic mapping (EHM) representation for MERG. Using entanglement based measures from quantum information theory and complex network theory, we study the emergence of topological order in the bulk of the EHM. We also demonstrate that the MERG is equivalent to a stabiliser quantum error correcting code. The MERG reveals very different holographic entanglement features for the normal metallic and topologically ordered states of the 2D Hubbard model, clarifying the essence of the entanglement phase transition that separates the two phases. We perform an information theoretic analysis of the EHM network, demonstrating that the information bottleneck principle is responsible for the distillation of entanglement features in the heirarchical structure of the EHM network. As a result, we construct a deep neural network (DNN) architecture based on our EHM network, and employ it for predicting the onset of topological order. We also demonstrate that the DNN is capable of distinguishing between the topologically ordered and gapless normal metallic phases.

---

[1]Corresponding author.

Contents

1 Introduction

Classifying quantum many-body systems at criticality, as well as away from it, based on entanglement features of the many-particle wavefunction is an outstanding challenge bearing implications for many-body theory, quantum information theory and quantum field theory [1–7]. The renormalization group (RG) formalism [8–10] is central to meeting this challenge,

as it involves characterizing various phases of matter and the phase transitions between them. Interpreting the RG length scale as an extra holographic dimension [11–17] has allowed the realization of $d+1$ dimensional space in the bulk by starting from a d dimensional quantum field theory at the boundary. Indeed, there has been a surge in the literature on the emergence of spatial geometry via the holographic renormalization of entanglement features [18–25] (e.g., mutual information, entanglement entropy) has been observed. Given that a diverse array of gapped and gapless quantum liquids can be studied via entanglement renormalization (ER) [26–33], it is imperative to ask the question: can we classify various quantum liquids solely based on the attributes of entanglement features generated via ER? Various kinds of entanglement RG (ERG) have been implemented in the recent past, mostly in terms of renormalisation schemes implemented on real space lattices. We review the construction of some of them here. The multiscale entanglement renormalization group ansatz (MERA) is a tensor network defined as the stacking of N transformation layers comprising unitaries and isometries acting on a system of 2^N qubits [4, 34, 35]. The input array of qubits at the d-dimensional *b*oundary (i.e., at the ultraviolet (UV) energy scale of the network) are in general entangled and comprise the initial many-body state. These input qubits are gradually transformed by a series of duplet layers stacked along the holographic RG direction from UV to infrared (IR) energy scales. Each of the duplet layers is composed of the following: layer 1 is a tensor product of (real space) local unitary disentangler gates with two input and two output legs each, while layer 2 is a product of isometries with two input legs and one output leg each. Layer 2 is, in essence, a projective transformation that removes the disentangled qubits generated at each RG step from the complete Hilbert space. As a result, the number of legs at the output from each layer is exactly half of the number of input legs. MERA and its other variants [36–38] allow the holographic generation of spatial geometry [19, 21–24, 39] along the RG direction, starting from a tensor network [40–42] representation of the many-body state it acts on. There is a generalization of MERA, i.e., the entanglement holographic mapping (EHM) [23, 24], in which each transformation layer is comprised of only unitaries (i.e., layer 1 discussed above). As a consequence, the EHM is also a tensor network formed from a collection of the unitary transformation layers. This should be contrasted with MERA, where only the many body states have a tensor network representation. In EHM, the disentangled qubits are present in the bulk, allowing a fuller description of the space-time geometry emergent via the RG flow. The time dynamics of the EHM tensor network is encoded in the inverse energy scales of the decoupled degrees of freedom included in its bulk, allowing for the computation of equal time, as well as unequal time, bulk correlators [24]. This demonstrates the equivalence of the EHM to a quantum renormalization group (QRG, see Ref. [24, 43] for recent attempts). As we will discuss below, in our implementation of the EHM via a unitary RG [44, 45], the appearance of an energy scale for quantum fluctuations naturally encodes the quantum dynamics of the emergent space.

An outstanding challenge for ERG has been in its application to strongly correlated electronic systems [46, 47]. Although there are several works on constructing tensor networks, e.g., MERA or EHM, for systems of noninteracting fermions [24, 46, 48], there are only a few on systems of interacting fermions [49, 50]. Thus, by and large, the implementation

of ERG on highly entangled systems resulting from strong electronic correlations remains unresolved. Our work thus aims for the construction a momentum-space entanglement renormalization group (MERG) [51] technique based on the unitary transformation based RG (URG) that has recently been applied to the 2D Hubbard model [44] and quantum XXZ kagome antiferromagnet [45]. At every step of the URG, we perform an unitary operation U that, similarly to QRG [24, 43], MERA and EHM systematically disentangles the electronic states at the UV from those at IR. This leads to the iterative block diagonalization of the Hamiltonian along the RG flow, approaching a model at the IR fixed point which is simpler than the bare model one started with. For the 2D Hubbard model at half-filling, we have obtained the Mott insulating ground state wavefunction analytically from the low-energy fixed point theory in Ref.[44]. The ground state manifold is found to be topologically degenerate [52], with a nonlocal Wilson loop as its stabilizer. We have also validated quantitatively the effective Hamiltonian and ground state wavefunction for the Mott insulator obtained from the URG procedure by benchmarking with high accuracy the ground state energy per particle, as well as the doublon fraction, against other numerical methods [53].

In the present work, the MERG scheme is implemented as a *reverse* unitary RG. Similar reverse RG approaches that involve the re-entangling of hitherto disentangled degrees of freedom has been discussed for some tensor network RG approaches [22, 54]. For this, we start from the many-body state at the IR fixed point, and approach the UV (i.e., towards the eigenstate of the parent model) by iterative applications of the inverse of the unitary transformations of the URG. The reconstruction method is validated by showing a reduction in the uncertainty of the energy eigenvalue of the reconstructed state with respect to that of the parent model. By representing the many-body states at each RG step as quantum circuits/tensor network [42], and by representing each unitary transformation step as a product of two-local universal gates [55], we obtain an equivalent EHM description for the MERG. Further, such a decomposition guarantees that URG is a version of a Clifford stabiliser code [56] that obeys the Gottesman-Knill theorem. Therefore, the reverse RG can be visualized as a entanglement RG flow along the reverse holographic direction [22, 24]. Much like the EHM, MERG is a version of MERA that preserves spectral weight during the RG flow [24]; this is precisely why we are able to implement both forward and reverse RG constructions. Importantly, note that at each RG step, the U transformations are not determined variationally as in MERA [35] or EHM. Instead, they are determined directly from the form of the Hamiltonian obtained at the previous step [44]. The URG procedure also encodes naturally an energy scale for quantum fluctuations (ω), accounting for the variation in entanglement content as well as the energy contributions of the decoupled states within the bulk of the tensor network. Thus, similar to EHM [24], the bulk correlation functions in the MERG are naturally time dynamical. It is also noteworthy that each transformation layer in MERG has a finite-depth that quantifies the circuit complexity of the corresponding unitary gate. This is in contrast with MERA, where every RG step has only unit depth. On the other hand, this aspect of MERG is similar to deep MERA (dMERA) [38], where every RG step has a finite depth D.

We will now discuss the entanglement features pertinent to the ERG program, and then

provide a comparative study with the features observed in MERG. One important property relates to the entanglement entropy of a region R in the input state at the UV scale $|\Psi\rangle$, i.e., the boundary of MERA or EHM tensor network. It was shown in Ref.[22] that the entanglement entropy is bounded from above by the number of legs that must be cut for the isolation of the region R from its complementary part. Upon descending further into the tensor network, the number of legs that need to be cut are reduced exponentially. The depth of the MERA/EHM quantum circuit/tensor network quantifies the circuit complexity of the state $|\Psi\rangle$, i.e., the minimum number of two-local and one-local universal gates required to obtain the entangled state from a separable state [57]. As we are disentangling qubits in the MERG program, the circuit complexity is greatly reduced in the bulk of the EHM. Therefore, the gain in efficiency in obtaining the entanglement features of a region R in $|\Psi\rangle$ is tied to the reduction in circuit complexity of state $|\Psi\rangle$ and the unitary transformation U. This attribute of the EHM conforms to the Ryu-Takayanagi formula [3], where the entanglement entropy of a region is determined by the minimal surface (whose length is the number of links cut) of the causal cone enveloping it [22, 58]. This observation motivates the manifestation of a holographic duality within the ERG framework [24]. In this work, we show that the EHM constructed from MERG has features similar to the Ryu-Takayanagi relation; indeed, we find that the entanglement entropy obtained by isolating a region R after every layer of transformation is bounded from above by the length of the minimal surface of the causal cone that surrounds it. We show that both the Mott insulating and the normal metallic states obtained from MERG respect the Ryu-Takayanagi relation. Further, we find that in MERG, the structure of the causal cone deep in the bulk of the EHM is determined by degrees of freedom residing close to the Fermi surface. This is similar to the finding that Fermi surface wave vectors play a crucial role in determining the entanglement entropy for gapless metallic quantum critical systems [59, 60].

Another essential feature of tensor networks such as EHM and MERA is that they encode the entanglement content of the many-body state geometrically [24, 39]. This can be quantified in terms of a distance measure such as the negative logarithm of the quantum mutual information (MI) between pairs of qubits (i, j). The lower the entanglement of the pair, the higher is the distance and vice-versa. Note that the information theoretic distance between a pair of qubits (i, j) obtained from the bulk of EHM is, in general, different from that obtained at the boundary, implying that a curved space-time geometry can be encoded into the EHM. For instance, an information theoretic distance proportional to the logarithm of the physical distance indicates the generation of hyperbolic space-time geometry from entanglement along the RG holographic direction [39]. We further note that while Ref.[61] established that the mutual information is an upper bound for various two-point correlation functions, it has been shown that that the *entanglement geometry* generated from MI asymptotically (i.e. deep within the tensor network) of the EHM encodes the single-particle bulk correlation function [24]. In the EHM obtained by us from the MERG, we compute the mutual information between pairs of pseudospins i and j (each of which is a composite of two single electron states in momentum-space with opposite spin). Upon approaching the Fermi energy in the bulk of our EHM, the MI is thus related to the four fermion bulk correlators of a system of interacting electrons, rather than the two

fermionic kind constructed from noninteracting degrees of freedom in the EHM of Ref.[24]. This indicates that our EHM encodes the spacetime geometry generated by the emergent degrees of freedom at low energies. We find that for the Mott insulator, the largest MI pertains to a singlet state formed by pseudospin pairs deep in the IR. This is also displayed by a finite correlation between the pseudospins in this particular case. On the other hand, we find that for a gapless metallic state, the correlation between momentum-space pseudospins vanishes in the IR. This is also reflected in our finding of a spacetime that collapses to a singularity in the IR for the insulating case, and a spacetime that expands for the metallic phase. While the former indicates the condensation of singlet pairs with real-space short-ranged entanglement in the Mott insulating state [44], the latter reflects on the scaling of the ERG towards a gapless Fermi surface [22, 24, 59]. Further, our findings appear to indicate that the metal-insulator transition between the Mott insulator and the gapless normal state acts as a horizon between the two entanglement spacetimes corresponding to these states, consistent with the suggestion of Ref.[17, 62]

We end by mentioning some applied aspects of our work. Both MERA and EHM have interpretations as quantum error correcting codes [63–66]: along the reverse holographic direction from IR to UV, the unitary transformation layer acts as an encoding map that re-entangles the stabiliser codeword (IR fixed point) with the (hitherto) disentangled degrees of freedom [67]. Conversely, the passage from UV to IR involves disentangelement of qubits at UV scale and acts a decoder of the stabiliser codeword in the IR. This has implication for fault tolerant quantum computing and topological quantum error correction codes [67–69]. In our present work, the codework space is formed by the two-fold topologically degenerate ground states of the Mott insulator , such that the forward (U) and reverse ($U^\dagger$) unitary transformations either distill the codeword space from the space of decoupled qubits, or spreads the entanglement content of the former across the latter. We demonstrate these error correction features of the MERG in this work. In this way, MERG provides a platform for designing noise resilient topological error correction [38, 70, 71]

A second important perspective of the MERG is as a deep neural network (DNN) architecture. We recall that a DNN generalisation of the restricted Boltzmann machine (RBM) is comprised of a stack of several hidden layers of neurons that generate simpler representations of the input data while preserving its essential features [72]. For example, an input data with N features (i.e., with a N-dimensional feature vector) undergoes dimensional reduction such that irrelevant features are discarded, and relevant features are distilled from one layer to the next. This has been demonstrated as being equivalent to the variational RG framework of Ref.[73, 74], where UV degrees of freedom are coarse-grained in an iterative fashion, thereby distilling the IR theory [75]. These works show that variational aspect of the Kadanoff RG is equivalent to the usage of training data in constructing the optimal weight matrices for the hidden layers of the DNN using the steepest descent algorithm. Tishby and Zaslavsky [76] have shown that such DNN architectures follow the Information Bottleneck (IB) principle: an optimally transformed representation of the input data is one in which the mutual information between the output and input data is reduced, while preserving the essential components of the target feature vector. Similarly, the disentangling and isometry layers of tensor networks such as MERA [77–79] lead to a lower-dimensional

representation of the original many-particle wavefunction they act on: the qubits disentangled at every layer are projected out, while preserving the entanglement features pertaining to degrees of freedom in the IR [80].

This suggests that the EHM of resulting from our MERG is equivalent to a unitary realisation of a DNN based purely on unitary transformations. As our MERG is based on analytic expressions for the unitary disentanglers of the URG formalism, the equivalent DNN does not need optimisation via a variational procedure. Indeed, we will demonstrate in this work that the MERG based DNN follows the optimal IB trajectory. Further, this allows for the holographic reconstruction of the many-body state of the parent Hamiltonian (i.e, input feature vector of the DNN/ UV boundary of the MERG tensor network) starting from the essential features obtained from the target vector (RG fixed point/ IR bulk of the MERG tensor network) by reversing the flow of information across the DNN. In this sense, the RG flow of the URG represents a supervised DNN [76], while the inverse RG flow represents a generative DNN [81, 82]. Recent works have highlighted similar relations between DNNs and tensor networks [83–85] on the one hand, and the holographic duals of DNNs [86]. Importantly, we construct a DNN based on the MERG that can classify Mott insulating and normal metallic phases by distinguishing their entanglement features. In this way, the DNN we construct is sensitive to the metal-insulator transition that lies between these two phases of quantum matter.

The rest of the work is organised as follows. In Section 2, we present the 2D Hubbard model briefly, as well as the unitary RG formalism of Ref.[44] that is pertinent to the present work. We then formulate the MERG scheme for the topologically ordered insulating ground state of the 2D Hubbard model in Section 3. This is followed by developing quantum circuit representation of the many-particle state as well as the renormalisation procedure, leading to a numerical validation of the MERG. We then present the entanglement holographic mapping (EHM) for the MERG, allowing for a study of the emergence of the topologically ordered ground state from the entanglement RG and its visulation as a quantum error correcting code. In Section 4, we compute the ERG flow using several measures of entanglement (e.g., mutual information), developing insight on the distinction between the entanglement signatures of a gapped insulating ground state and a gapless normal metallic state. Finally, in Section 5, we use the EHM to develop a deep neural network that can classify the insulating and metallic phases based on their entanglement features. We conclude in Section 6. Some details of the URG method and properties of the normal metallic phase are presented in two appendices.
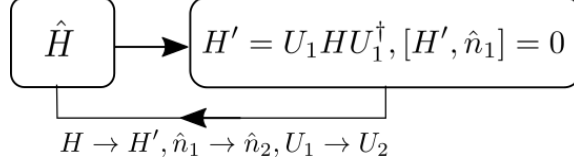
2 Preliminaries

2.1 The model

The 2D Hubbard model on a square lattice at 1/2-filling, with nearest neighbour hopping (strength t) and on-site Hubbard repulsion (strength U_0), is described by the Hamiltonian

$$\hat{H} = \sum_{\mathbf{k},\sigma} \epsilon_{0\mathbf{k}} c^{\dagger}_{\mathbf{k}\sigma} c_{\mathbf{k}\sigma} + U_0 \sum_{\mathbf{r}} \hat{\tau}_{\mathbf{r}\uparrow}\hat{\tau}_{\mathbf{r}\downarrow} , \tag{2.1}$$

Figure 1. Schematic diagram of the iterative unitary RG procedure. Each RG step generates a number occupation operator $\hat{n}_1$ that commutes with the Hamiltonian.

where $c_{\mathbf{k}\sigma}^{\dagger}/c_{\mathbf{k}\sigma}$ are the electron creation/annihilation operator with wave-vector $\mathbf{k}$ and spin σ. The operator $\hat{\tau}_{\mathbf{r}\sigma} = \hat{n}_{\mathbf{r}\sigma} - \frac{1}{2}$, where $\hat{n}_{\mathbf{r}\sigma} = c_{\mathbf{r}\sigma}^{\dagger}c_{\mathbf{r}\sigma}$ is the number operator at lattice site $\mathbf{r} = j_1\hat{x} + j_2\hat{y}$ and $\epsilon_{0\mathbf{k}}$ is the bare dispersion. The hopping term is number diagonal in momentum-space, with a dispersion $\epsilon_{0\mathbf{k}} = -2t(\cos k_x + \cos k_y)$. On the other hand, the Hubbard repulsion term is diagonal in position space, and is therefore off-diagonal in the momentum basis. This is responsible for quantum fluctuations in the one particle dispersion $(\Delta(\epsilon_{\mathbf{k}\sigma}\hat{n}_{\mathbf{k}\sigma}))$. Below, we lay out the unitary renormalization group procedure introduced in Ref.[44] that block diagonalizes the Hamiltonian by recursively resolving the quantum fluctuations.

2.2 Unitary Renormalization Group

In an earlier work [44, 87], we introduced a unitary operator based RG that block diagonalizes the Hamiltonian iteratively and performs a systematic disentanglement of electronic degrees of freedom in the associated eigenspace. A typical workflow of this unitary RG procedure is given in Fig.1(see Appendix A for derivation of the unitary operator), such that the (n)th step involves a unitary operation $U_{(n)}$ given by

$$U_{(n)} = \frac{1}{\sqrt{2}}(1 + \eta_{(n)} - \eta_{(n)}^{\dagger})$$
$$\eta_{(n)}^{\dagger} = \frac{1}{\hat{\omega}_{(n)} - Tr_n(H_{(n)}^D \hat{n}_n)\hat{n}_n} c_n^{\dagger} Tr_n(H_{(n)}c_n) . \tag{2.2}$$

The operators $\eta_{(n)}$, $\eta_{(n)}^{\dagger}$ fulfil the algebra $\{\eta_{(n)}, \eta_{(n)}^{\dagger}\} = 1$, $[\eta_{(n)}, \eta_{(n)}^{\dagger}] = 1 - 2\hat{n}_{(n)}$. The operator $\hat{\omega}_{(n)}$ in the expression for $\eta_{(n)}^{\dagger}$ accounts for the residual quantum fluctuations due to remnant entanglement in the rotated eigenspace, and is defined as

$$\hat{\omega}_{(n)} = H_{(n-1)}^D + H_{(n-1)}^X - H_{(n)}^X , \tag{2.3}$$

where $H_{(n)}^D$ and $H_{(n)}^X$ represents the diagonal and the off diagonal components of $H_{(n)}$. Furthermore, the good occupation quantum numbers of the disentangled electronic states label the Hamiltonian's eigenstates in the rotated eigenspace. The eigenvalues ω's of $\omega_{(n)}$ form the natural quantum energyscale, generating multiple effective Hamiltonian RG flows such that, at each scale, a subpart of the complete Hamiltonian spectrum is renormalized as well as block diagonalised.

We adapt the RG procedure to the 2D Hubbard model by setting up a labelling scheme for the states in momentum space. The states are labelled by two indexes: distance Λ

$$W \xrightarrow{\quad\text{MFL}\quad|\ \text{PG}\quad|\ \text{ML}\ } 0$$
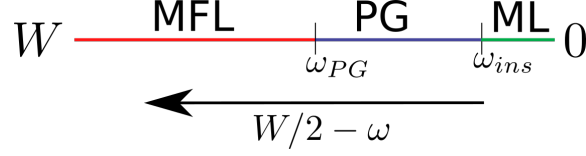
Figure 2. Schematic representation of the $T = 0$ RG phase diagram of the 2D Hubbard model at $1/2$-filling as a function of quantum fluctuation energyscale $(4 - \omega)$. Red, blue and green regions represent the marginal Fermi liquid metal (MFL), pseudogap (PG) and the Mott insulating liquid (ML) phases respectively. ω_{PG} and ω_{ins} are energy scales for transitions that initiate and end the PG phase.

from the noninteracting Fermi surface ($\epsilon_{\mathbf{k}} = 0$, FS), and the direction normal to the FS ($\hat{s} = \frac{\nabla \epsilon_{\mathbf{k}}}{|\nabla \epsilon_{\mathbf{k}}|}|_{\epsilon_{\mathbf{k}} = E_F}$) such that $\mathbf{k}_{\Lambda\hat{s}} = \mathbf{k}_{F\hat{s}} + \Lambda\hat{s}$. This unveils a natural scheme for labelling the states in terms of distances $\Lambda_N > .. > \Lambda_j > \Lambda_{j-1} > .. > 0$. The RG transformations then disentangle electronic states farthest from the FS, gradually scaling towards Fermi energy E_F. At step j, all the states on the curve Λ_j are completely disentangled via a unitary rotation $U_{(j)}$. The resulting Hamiltonian $H_{(j-1)} = U_{(j)} H_{(j)} U_{(j)}^\dagger$ is off-diagonal only for states residing within a window $\Lambda < \Lambda_j$ around the erstwhile FS. The disentanglement of an entire curve at distance Λ_j is represented via a product of unitary rotations $U_{(j)} = \prod_{l \in (\hat{s}, \sigma = \uparrow/\downarrow)} U_{(j,l)}$, where $U_{(j,l)}$ disentangles one state $\mathbf{k}_{\Lambda_j\hat{s}}\sigma$ on the curve Λ_j. The form of $U_{(j,l)} = \frac{1}{\sqrt{2}}[1 + \eta_{(n)} - \eta_{(n)}^\dagger]$ where $n = (j,l)$ and $\eta_{(n)}$, $\eta_{(n)}^\dagger$ have the same definitions as presented in eq.(2.2).

2.3 Normal and topologically ordered (T.O.) insulating phases of the 2D Hubbard model at $1/2$-filling

The renormalization procedure reveals a marginal Fermi liquid (MFL) gapless metallic phase [44, 87] (red region in the schematic phase diagram Fig.2) in the quantum fluctuation energy range $W > \frac{W}{2} - \omega > \frac{W}{2}$. The Hamiltonian for the MFL is found to be

$$H_1^* = \sum_{j,l} \epsilon_{j,l} \hat{n}_{j,l} + \frac{1}{8} \sum_{j,j',l} R_{ll'}^* \hat{n}_{j,l} \hat{n}_{j,l'} (1 - \hat{n}_{j',l}) \ , \tag{2.4}$$

where $j, l = \Lambda_j, \hat{s}, \sigma$ and $j, l' = -\Lambda + \delta, T\hat{s}$. The first and second terms in Hamiltonian eq.2.4 describes the 1 particle and 2 particle-1 hole dispersions respectively. The 2 particle-1 hole dispersion $R_{ll'}^* = \omega - 1/2(\epsilon_{j*,l} + \epsilon_{j*,l'})$ arises from the interplay between forward scattering processes involving electronic pairs with different net momentum. About the fluctuation scale $\frac{W}{2} - \omega_{ins}$, the system undergoes a transition into a Mott insulating phase (green region in the phase diagram Fig.2) described by the fixed point Hamiltonian

$$\hat{H}_2^* = \sum_{\hat{s}} K_{\hat{s}}^* \left[\mathbf{A}_{*,\hat{s}} \cdot \mathbf{A}_{*,-\hat{s}} - \mathbf{S}_{*,\hat{s}} \cdot \mathbf{S}_{*,-\hat{s}} \right] \ , \tag{2.5}$$

where the charge and spin type psuedospins within the emergent fixed point window $\Lambda_{\hat{s},\omega}^*$, $\mathbf{A}_{*,\hat{s}}$ and $\mathbf{S}_{*,\hat{s}}$ respectively, are defined as

$$\mathbf{A}_{*,\hat{s}} = \sum_{\Lambda < \Lambda_{\hat{s},\omega}^*} \mathbf{A}_{\Lambda,\hat{s}} \ , \mathbf{S}_{*,\hat{s}} = \sum_{\Lambda < \Lambda_{\hat{s},\omega}^*} \mathbf{S}_{\Lambda,\hat{s}} \ , \mathbf{A}_{\Lambda,\hat{s}} = f_{\Lambda,\hat{s}}^{c;\dagger} \frac{\boldsymbol{\sigma}}{2} f_{\Lambda,\hat{s}}^c \ , \mathbf{S}_{\Lambda,\hat{s}} = f_{\Lambda,\hat{s}}^{s;\dagger} \frac{\boldsymbol{\sigma}}{2} f_{\Lambda,\hat{s}}^s \ , \tag{2.6}$$

– 8 –

where $f^{c;\dagger}_{\Lambda,\hat{s}} = \left[c^{\dagger}_{\Lambda,\hat{s},\sigma} \, c_{-\Lambda,T\hat{s},-\sigma}\right]$ and $f^{s;\dagger}_{\Lambda,\hat{s}} = \left[c^{\dagger}_{\Lambda,\hat{s},\sigma} \, c^{\dagger}_{\Lambda-2\Lambda^{*}_{\hat{s}},T\hat{s},-\sigma}\right]$ are the spinorial representation for a pair of electrons. $K^{*}_{\hat{s}}$ is the final magnitude of the backscattering coupling. The degenerate ground state configurations of the Mott insulating phase are labelled by the eigenvalues of the three operators $\mathbf{A}_{*} = \mathbf{A}^{*}{}_{\hat{s}} + \mathbf{A}^{*}{}_{-\hat{s}}$, $\mathbf{A}^{*}{}_{\hat{s}}$ and $\mathbf{A}^{*}{}_{-\hat{s}}$, *or* their $\mathbf{S}$ counterparts

$$|\Gamma_{+}\rangle = |A_{*} = 0, A^{*}_{\hat{s}} = A^{*}_{-\hat{s}} = N^{*}_{\hat{s}}, S_{\Lambda\hat{s}} = 0\rangle \ , \ |\Gamma_{-}\rangle = |S_{*} = 0, S^{*}_{\hat{s}} = S^{*}_{-\hat{s}} = N^{*}_{\hat{s}}, A_{\Lambda\hat{s}} = 0\rangle \ . (2.7)$$

The two configurations $|\Gamma_{+}\rangle$ and $|\Gamma_{-}\rangle$ are constructed such that first is an eigenstate of the 1st term in H^{*}_{2} (and has null contribution from the 2nd term), while $|\Gamma_{-}\rangle$ is the eigenstate of the 2nd part (and has no contribution from the first). Importantly, we note that the true degeneracy between these ground states is only achieved in the thermodynamic limit. The RG procedure has been validated [44] by benchmarking the ground state energy per site of the 1/2-filled Hubbard model against other numerical methods across values of U's with magnitudes ranging from weak to strong [53]

To characterize the topological features of the gapped two degenerate subspaces, we construct a nonlocal operators W

$$W = \exp\left[i\frac{\pi}{2}(|\Gamma_{+}\rangle\langle\Gamma_{+}| - |\Gamma_{-}\rangle\langle\Gamma_{-}| - 1)\right] \ . \tag{2.8}$$

W commutes with the $SU(2) \times SU(2)$ pseudospin rotational invariant Hamiltonian H^{*}_{2} in the projected subspace of the states $|\Gamma_{+}\rangle$ and $|\Gamma_{-}\rangle$. The two degenerate ground states are adiabatically connected via a twist operator/ nonlocal gauge transformation $\hat{O}|\Gamma_{\pm}\rangle = |\Gamma_{\mp}\rangle$. As these two states are protected by a many body gap, adiabatic passage between these degenerate ground states involve the creation of charge-1/2 excitations [52, 88, 89]; this is seen from the anticommutation relation $\{O, W\} = 1$. Similar twist-translation relation operator relations have also been found recently by some of us for quantum liquid ground states in frustrated quantum antiferromagnets [90, 91]. In the next section, we introduce the entanglement renormalization scheme using the unitary transformations eq.(2.2). This will reveal nontrivial entanglement features of gapped topological order, as well as distinguishing it from a gapless state of matter.

3 MERG construction for the topologically ordered insulating ground state of the 2D Hubbard model

The ground state wavefunction of a parent model such as the 2D Hubbard model is in general difficult to obtain. However, once available, it allows for the computation of various correlation functions for, e.g., characterizing the low energy features of the system as being either gapless or gapped. We will now demonstrate how this task can be carried out for the 2D Hubbard model using the unitary renormalization group (URG) method. We have already seen above that the URG approach can be carried out in a non-perturbative manner, helping obtain stable fixed point theories at which the RG flows terminate. Further, the stable fixed point Hamiltonians (eq.2.5) are comparatively easier to solve either analytically or numerically than their parent model counterparts [92].

Thus, the precise program we follow is this (see also Fig.3). We begin by implementing the URG [87] by applying a sequence of unitary transformations to the parent Hamiltonian H.
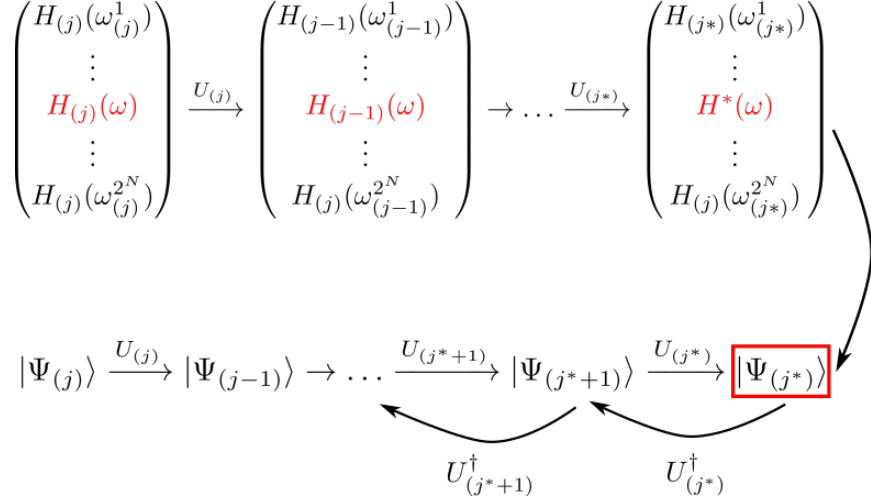
Figure 3. Upper row: URG flow scheme for Hamiltonians, terminating at fixed point Hamiltonians, e.g. $H^*(\omega)$, characterised by fluctuation energy scale ω. Lower line: entanglement renormalization RG flow constructed via the inverse unitary transformations $U^\dagger_{(j^*+n)}s$ on the eigenstate $|\Psi^*\rangle$ (red bordered box) of $H^*(\omega)$.

As demonstrated above, successive unitary transformations lead to a fixed point Hamiltonian $H^*(\omega)$ and its ground eigenstate $|\Psi^*\rangle$ at a given quantum fluctuation scale ω. Now, by reversing the unitary transformation, we can reconstruct the (a priori unknown) ground eigenstate $|\Psi\rangle$ of the parent model.

In this way, we realize URG as a momentum space entanglement renormalization group (MERG) procedure carried out for the 2D Hubbard model. This involves constructing a toy model for the fixed point theory, H^*, with 4 outward directions normal to the FS, $\hat{s}_1 = (\pi/4, 3\pi/4)$, $\hat{s}_2 = (\pi/2, \pi/2)$, $\hat{s}_3 = (-\pi/4, -3\pi/4)$ and $\hat{s}_4 = (-\pi/2, -\pi/2)$, and with 56 electrons that pair up into 28 pseudospins. The pseudospin states are labelled as follows (see Fig.4): the states labelled $0, ..., 6$ are along $\hat{s}_1$, $7, ..., 13$ are along $\hat{s}_2$, $14, ..., 20$ are along $\hat{s}_3$ and $21, ..., 28$ are along $\hat{s}_4$. Next, we prepare the system in the eigenstate $|\Gamma_+\rangle$ of the Hamiltonian H_2^*. We consider here a simple construction of $|\Gamma_+\rangle$ (see Fig.4): two pair of singlets formed out of pair of backscattering pseudospins $(6, 20)$ (involving $\hat{s}_1$ and $\hat{s}_3$) and $(13, 27)$ (involving $\hat{s}_2$ and $\hat{s}_4$). The black/white circles in Fig.4 represent up/down configurations of the disentangled pseudospins. Altogether, $|\Gamma_+\rangle$ is represented as

$$|\Gamma_+\rangle = \frac{1}{2} \prod_{n=[0,3]} \prod_{\substack{i=[7n,7n+2], \\ j=[7n+3,7n+5]}} |0_i 1_j\rangle (|1_6 0_{20}\rangle - |0_6 1_{20}\rangle)(|1_{13} 0_{27}\rangle - |0_{13} 1_{27}\rangle) , \qquad (3.1)$$

and where we have $N = 6$ pseudospins along each of the four $\hat{s}_i$ directions normal to the FS. The two singlets that comprise the initially entangled subspace can be seen from the second and third terms above, while the product of $|0_i 1_j\rangle$ states correspond to the disentangled pseudospin states.

We now reintroduce the dominant quantum fluctuations in the state $|\Gamma_+\rangle$ in the form of tangential scattering, forward scattering and backscattering processes via the successive

application of the reverse unitary maps $U^{\dagger}_{(j*+n)}$ (see Fig.3). Importantly, we note that the fluctuations are being added only within the projected subspace of charge pseudospins. We note that for this specific case, the unitary operation $U_{(j)}$ disentangles 4 pseudospins labelled $n(N+1) + N - j$ and where $n = 0, 1, 2, 3$ is index for the four normal directions and there are $N = 6$ pseudospins along each normal direction

$$U_{(j)} = U_{4N-j+3}U_{3N-j+2}U_{2N-j+1}U_{N-j}. \tag{3.2}$$

In the above, $U_{n(N+1)+N-j}$ disentangles the pseudospin along the normal $\hat{s}_{n+1}$ at distance $\Lambda_{n(N+1)+N-j}$ from the reference non interacting FS, and is defined as follows

$$U_{n(N+1)+N-j} = \frac{1}{\sqrt{2}} \left[1 + A^-_{n(N+1)+N-j} \frac{1}{\hat{\omega} - H^D_{1(j)}} C_j B^+_j - A^+_{n(N+1)+N-j} \frac{1}{\hat{\omega} - H^D_{0(j)}} C_j B^-_j \right], \tag{3.3}$$

where $\mathbf{B}_j = \begin{pmatrix} \mathbf{A}_{0j} & \mathbf{A}_{1j} & \mathbf{A}_{2j} & \mathbf{A}_{3j} \end{pmatrix}^T$, $\mathbf{A}_{nj} = \sum_{l=1}^{N+1} \mathbf{A}_{nl+N-j}$ and the coupling matrix

$$C_j = \begin{pmatrix} V_1^{(j)} & L^{(j)} & K_1^{(j)} & 0 \\ L^{(j)} & V_2^{(j)} & 0 & K_2^{(j)} \\ K_1^{(j)} & 0 & V_1^{(j)} & L^{(j)} \\ 0 & K_2^{(j)} & L^{(j)} & V_2^{(j)} \end{pmatrix}. \tag{3.4}$$

$H^D_{1(j)}$ and $H^D_{0(j)}$ are the diagonal parts of the Hamiltonian in the projected subspaces of $\uparrow/\downarrow$ configurations of pseudospin j, e.g.,

$$H^D_{1(j)} = \sum_{\substack{l=1, \\ i=[1,4]}}^{j} \epsilon_{\Lambda_l \hat{s}_i} A^z_{\Lambda_l \hat{s}_i} + B^z_j C B^z_j \tag{3.5}$$

In the coupling matrix, $V_{(j)}$, $L_{(j)}$ and $K_{(j)}$ are forward (purple line), backward (orange line) and tangential (green line) scattering couplings respectively displayed in Fig.4. Finally, the MERG flow equation is given by
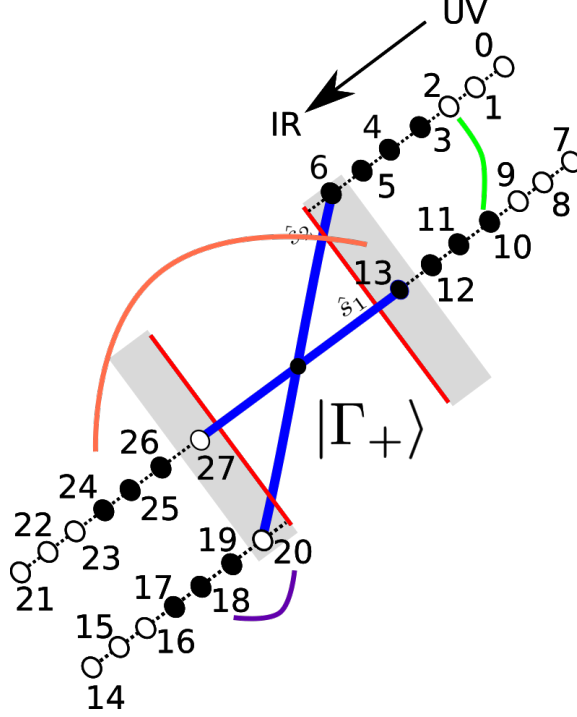
$$H_{(j)} = U^{\dagger}_{(j)} H_{(j-1)} U_{(j)}, \tag{3.6}$$

where the renormalized Hamiltonian

$$H_{(j)} = \mathbf{B}_j C_j \mathbf{B}_j^T. \tag{3.7}$$

From the MERG equation (eq.(3.6)) and $U_{(j)}$ (eq.(3.3))(l=1,2), we obtain the coupling RG equations accounting for the quantum fluctuations arising from the scattering of a pseudospin pair

$$V_l^{(j-1)} = V_l^{(j)} + \frac{(V_l^{(j)})^2}{\frac{1}{2}(\epsilon_{\Lambda_j \hat{s}} + \epsilon_{\Lambda_j - \hat{s}}) - \omega - \frac{1}{4}V_l^{(j)}},$$

$$K_l^{(j-1)} = K_l^{(j)} + \frac{(K_l^{(j)})^2}{\omega - \frac{1}{2}(\epsilon_{\Lambda_j \hat{s}} + \epsilon_{\Lambda_j - \hat{s}}) - \frac{1}{4}K_l^{(j)}},$$

$$L^{(j-1)} = L^{(j)} + \frac{N_F^2 (L^{(j)})^2}{\frac{1}{2N'}\sum_s(\epsilon_{\Lambda_{j-1} \hat{s}} + \epsilon_{\Lambda_j - \hat{s}}) - \omega - \frac{1}{4}L^{(j)}}. \tag{3.8}$$

Figure 4. Representation of the ground state in the MERG construction. The blue lines indicate the singlets formed out of pairs of pseudospins $(6, 20)$ and $(13, 27)$. Dark/white circles represent up/down pseudospins. The arrow labelled UV to IR depicts the high to low variation of the pseudospin dispersion. The orange, green and purple arrows represents the backscattering, tangential scattering, forward scattering processes respectively.

In the above, $l = 1, 2$ represents the two normal directions $\hat{s}_1$ and $\hat{s}_2$. Additionally, note that we choose $W/2 - \omega = 0$ in implementing the MERG procedure, corresponding to the lowest quantum fluctuation (QF) scale lying well within the Mott insulating phase shown in the phase diagram Fig.2. For the QF energy $W/2 - \omega = 0$, the V and L vertices are RG irrelevant (eq.(3.8)), while the K backscattering vertices are RG relevant leading to the effective Hamiltonian H_2^* (eq.(2.5)).

In the next subsection, we will represent the fixed point ground state Γ_+, as well as the sequence of states $|\Psi_{(j)}\rangle's$ connected to it via $U_{(j)}^\dagger$'s, as many-body quantum circuits. As quantum circuits are very generally known to be examples of tensor networks [42, 77], this will help us realize a momentum space tensor network renormalization scheme for the MERG procedure.

3.1 Quantum circuit network representation of the T.O. ground state and its renormalization

As seen above, the many body ground state $|\Gamma_+\rangle$ at the RG fixed point has a simple entanglement structure involving only two maximally entangled pairs (Fig.3). As can be seen in Fig.5, this allows a easily computable quantum circuit description involving two controlled not (C-NOT) gates acting between pseudospins (6,20) and (13,27), such that
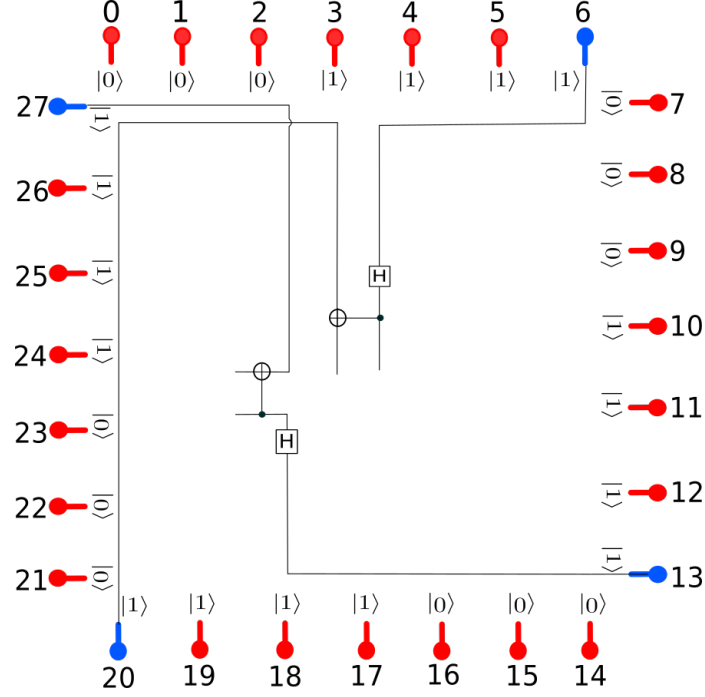
Figure 5. Quantum circuit representation of $|\Gamma_+\rangle$ in terms of one- and two-pseudospin gates.

the first pseudospin in each bracket (6 and 13) is a target bit and the second (20 and 27) a control bit. The Hadamard gate H acts on the control bit, rotating its state $|1\rangle$ to $\sqrt{2^{-1}}(|0\rangle - |1\rangle)$. This is followed by a C-NOT gate acting on 20 and 27, leading to the singlet states (blue qubits in Fig.3) in eq.(3.1). The disentangled states (red qubits in Fig.3) have either up or down spin configurations, as represented in eq.(3.1).

The quantum circuit description for the states generated via reverse RG is (Fig.3)

$$U_{(j)}^\dagger |\Psi_{(j-1)}\rangle = |\Psi_{(j)}\rangle \;, \tag{3.9}$$

and can be obtained via a decomposition of $U_{(j)}$ eq.(3.2) as a product of one/two qubit gates[55]

$$
\begin{aligned}
U_{(j)} &= U_{4N-j+3} U_{3N-j+2} U_{2N-j+1} U_{N-j} \\
U_\alpha &= U_{\alpha,N} \otimes U_{\alpha,N-1} \otimes \ldots \otimes U_{\alpha,N-j-1} \otimes U_{\alpha,2N+1} \otimes U_{\alpha,2N} \otimes \ldots \otimes U_{\alpha,2N-j} \otimes U_{\alpha,3N+2} \otimes \\
&\quad \otimes U_{\alpha,3N+1} \otimes \ldots \otimes U_{\alpha,3N-j+1} \otimes U_{\alpha,4N+3} \otimes U_{\alpha,4N+2} \otimes \ldots \otimes U_{\alpha,4N+2-j} H_\alpha \;, \tag{3.10}
\end{aligned}
$$

where $\alpha = n(N+1) + N - j$, n=0,1,2,3 and $N = 6$. The above decomposition of the unitary circuit into two local CNOT gates, Hadamard gates and phase gates implies that URG is a version of a Clifford stabiliser code [56] that obeys the Gottesman-Knill theorem, i.e., such a quantum circuit can be simulated on a classical computer in polynomial time. The unitary transformation U_{N-j} disentangles qubit labelled $N - j$ (see Fig.4 for the state labels), with similar definitions for the other unitary transformations. H_α represents the Hadamard gate. The individual two qubit gates $U_{n(N+1)+N-j,m(N+1)+N-l}$ can be represented via a controlled-U rotation with $\alpha = n(N+1) + N - j$ as the control bit and
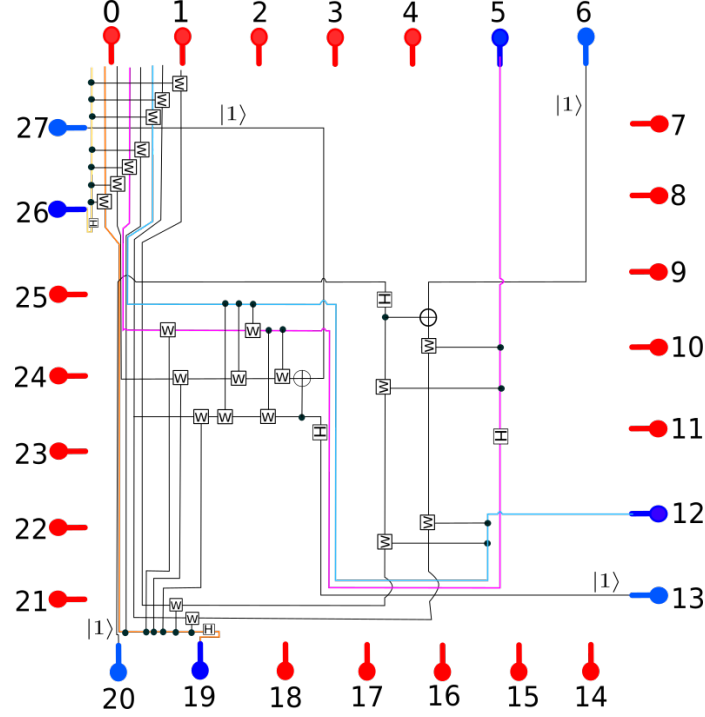
Figure 6. Quantum circuit representation of the many-body state after 1 reverse RG step in terms of one- and two-pseudospin gates. The purple, cyan, orange and yellow lines represent the entangling pathways of the qubits/pseudospins indexed 5, 12, 19 and 26.

$\beta = m(N + 1) + N - l$ as the target bit

$$U_{\alpha,\beta} = \frac{1}{\sqrt{2}} \left[|1_\alpha\rangle\langle 1_\alpha| \otimes W_\beta + |0_\alpha\rangle\langle 0_\alpha| \otimes I_2 \right] . \tag{3.11}$$

The form of the single qubit rotation operations, $W_\beta = \exp\left(\frac{i}{2}\boldsymbol{\sigma_\beta} \cdot \hat{\mathbf{n}}\right)$, can be obtained by solving the reverse RG eq.(3.9) using the decomposition of the unitary operator eq.(3.10) and the following representation of the $|\Psi_{(j)}\rangle$

$$|\Psi_{(j)}\rangle = a|1_{n(N+1)+N-j}\rangle|\Phi\rangle + b|0_{n(N+1)+N-j}\rangle|\chi\rangle , \tag{3.12}$$

where 1 and 0 represent the configurations of the pseudospin labelled $n(N + 1) + N - j$. The states $|\Phi\rangle$ and $|\chi\rangle$ represent the configurations of the rest of the pseudospins. The quantum circuit representation for the state $|\Psi_{(j^*+1)}\rangle$ is shown in Fig.6. The number of one/two-local unitary gates needed to obtain the quantum circuit description of the state $|\Psi_{(j^*+n)}\rangle$ quantifies the circuit complexity (CC) [57]. The CC for the circuit designs of $|\Psi_{(j)}\rangle$ at every RG step is found to be

$$CC(j) = 8j^2 - 2j - 4 . \tag{3.13}$$

In Figures 5 and 6, the quantum circuit description for the states $|\Psi_{(1)}\rangle$ and $|\Psi_{(2)}\rangle$ are thus found to possess the circuit complexity $CC(1) = 2$ and $CC(2) = 22$ respectively. By using the many body states generated via the reverse RG steps discussed earlier, the variation
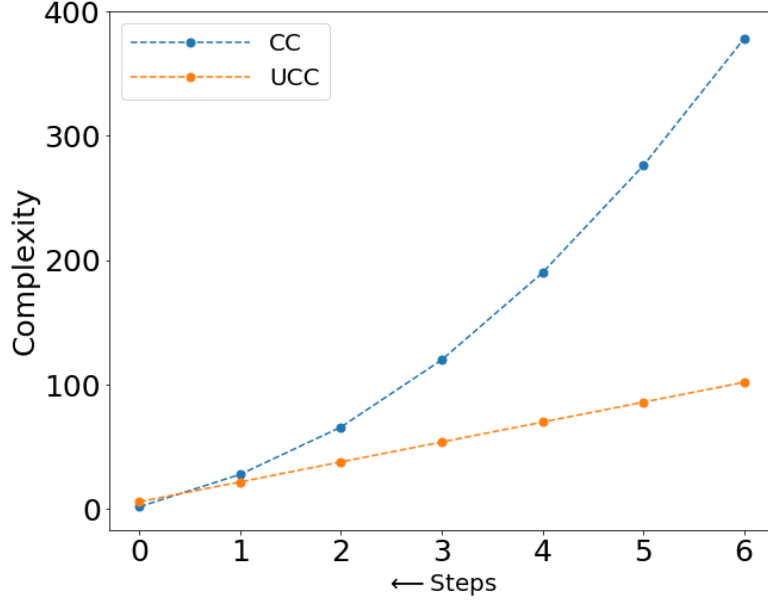
Figure 7. Orange curve CC represents circuit complexity of the many-body state, blue curve UCC represents complexity of the unitary transformation U (or equivalently D depth of U) along the RG flow trajectory.

of the circuit complexity along the RG flow is numerically verified by the blue curve in Fig.7. The orange curve in Fig.7 represents the decrement in complexity of the unitary disentangling operation at every RG step. With this construction, we have established MERG as a quantum circuit/tensor network renormalization group scheme. In the next subsection, we validate the RG formalism by displaying its capability in reconstructing the ground state of the parent model from the effective model.

3.2 Validation of the MERG scheme

MERG, being a unitary map involving inverse unitary transformations on the eigenstates of the effective model, should allow us to reconstruct the eigenstates of the parent Hubbard model. In this work, we account for only the dominant fluctuations in the charge pseudospin subspace of the operators. Deviation of the various pseudospin scattering couplings K, V, and L from a uniform magnitude of $U_0 =$ of the parent model can be clearly seen in eq.(3.7). Upon reversing the RG steps, this deviation should decrease. We quantify this decrease through the reduction in the pseudospin interaction energy fluctuations in the entangled subspace $\Delta E_{(j)} = \langle \Psi_{(j)} | (\Delta H_j)^2 | \Psi_{(j)} \rangle$ (see Fig.8). After six reverse RG steps, the fluctuations have already reduced to 10% of their initial value (see Fig.8), thereby validating the MERG approach.
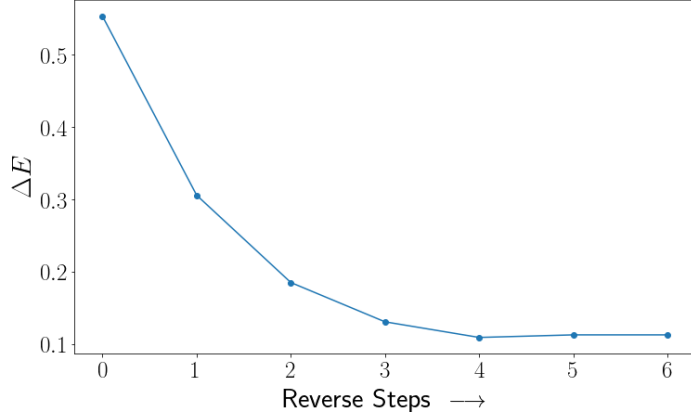
Figure 8. Plot displaying the reduction in energy uncertainty ΔE (with onsite repulsion $U_0 = 8$) upon reversing the RG steps.

3.3 Entanglement holographic mapping (EHM) representation for the topologically ordered phase

In the earlier section, we have established the URG procedure as a tensor network RG by providing quantum circuit description of many-body states [42]. In Fig.9, we describe the architecture of the tensor network RG through an equivalent entanglement holographic mapping (EHM) representation [23, 24]. Similar to the case of spectrum bifurcation renormalization group (SBRG) [93], unitary maps preserves the canonical fermion anticommutation relations.

At each RG step shown in Fig.9, the nonlocal unitary operator (yellow block in Fig.9) disentangles four pseudospins in the *holographic boundary* at high energies (UV), mapping them onto the red *emergent bulk physical qubits* at lower energies (i.e., towards IR). The first layer of unitary transformation disentangles the pseudospins located farthest from the FS (labelled $0, 7, 14, 21$), the next step pseudospins distentangled the pseudospins $1, 8, 15, 22$ and so on, eventually scaling towards the FS. Alongside these disentanglement RG steps, the pseudospins belonging to the entangled space undergo entanglement resharing. Deep in the IR regime, the system enters into an Mott liquid phase characterized by pseudospins pairing up as singlets (the dotted ovals pairing pseudospins $(6,20)$ and $(13,27)$ in Fig.9).

Similar to our earlier discussions, an important feature of the nonlocal unitary operation $U_{(j)}$ (yellow block in Fig.9) is that it can be decomposed as a product of local 2-qubit disentanglers. Below we present the decomposition for the operator U_{N-j}

$$U_{(j)} = U_{4N-j+3}U_{3N-j+2}U_{2N-j+1}U_{N-j}$$
$$U_{N-j} = U_{N-j,N} \ldots U_{N-j,N-j+1}U_{N-j,2N+1} \ldots U_{N-j,2N-j+1}U_{N-j,3N+2} \ldots U_{N-j,3N+2}$$
$$\times \, U_{N-j,4N+3} \ldots U_{N-j,4N-j+3} \, . \tag{3.14}$$

As an outcome of the complete transformation $U_{(j)}$, the four pseudospins labelled $N - j, 2N - j + 1, 3N - j + 2, 4N - j + 3$ are disentangled, and the *circuit complexity* of the
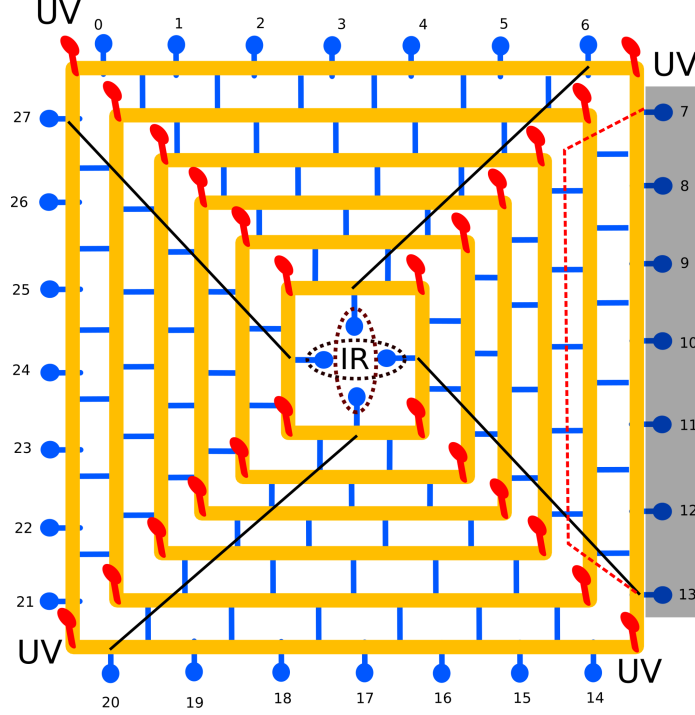
Figure 9. Entanglement holographic mapping (EHM) representation of MERG. The blue legs represent the holographic boundary made of the physical pseudospin qubits. The yellow block represents a nonlocal unitary disentangler which iteratively maps the boundary (blue) qubits to the bulk (red) qubits. The black lines represent the passage of the qubits $6, 13, 20, 27$ from UV to IR. The grey box represents the boundary region $7 - 13$ in the UV that is isolated within the bulk of the EHM by the the minimal surface/causal cone (dashed red line) after the second RG step.

unitary transformation is given by $UCC_j = 16j - 10$. It is interesting to note that the circuit complexity for the tensor network representation of the MERG quantum circuit ($UCC_j \sim O(j)$) is substantially less than that of the tensor network representation of the quantum state itself ($CC \sim O(j^2)$).

We now present an algorithm for obtaining the form of the individual disentangler $U_{\alpha,\beta}$ (where $\alpha = N - j, \beta = N$). For the RG step j, $|\Psi_{(j)}\rangle$ is the input state and $U_{(j)}|\Psi_{(j)}\rangle = |\Psi_{(j-1)}\rangle$ is the rotated output state. We first perform a decomposition of both the input and output states in terms of the up (1)/down (0) spin basis states labelled α, β and the subsystem configuration of the rest of the pseudospins

$$|\Psi_{(j)}\rangle = \sum_{m,n=[1,n_{max}]} D_{\alpha,\beta}^{m,n,(j)} |m\rangle_{\alpha,\beta} |\Phi_{(j)}^n\rangle \ ,$$

$$|\Psi_{(j-1)}\rangle = \sum_{m',n'=[1,n'_{max}]} D_{\alpha,\beta}^{m',n',(j-1)} |m'\rangle_{\alpha,\beta} |\Phi_{(j-1)}^{n'}\rangle \ . \tag{3.15}$$

Here, the states $|\Phi_n\rangle$ and $|m\rangle$ are orthonormalized, with m belonging to the configuration set of two pseudospins $m \in \{00, 01, 10, 11\}$. Additionally, we note that in the state $|\Psi_{(j-1)}\rangle$, the configuration of pseudospin α is restricted to 0 or 1; this restricts m' to one of the two subsets $m' \in \{00, 01\}$ and $m' \in \{10, 11\}$.
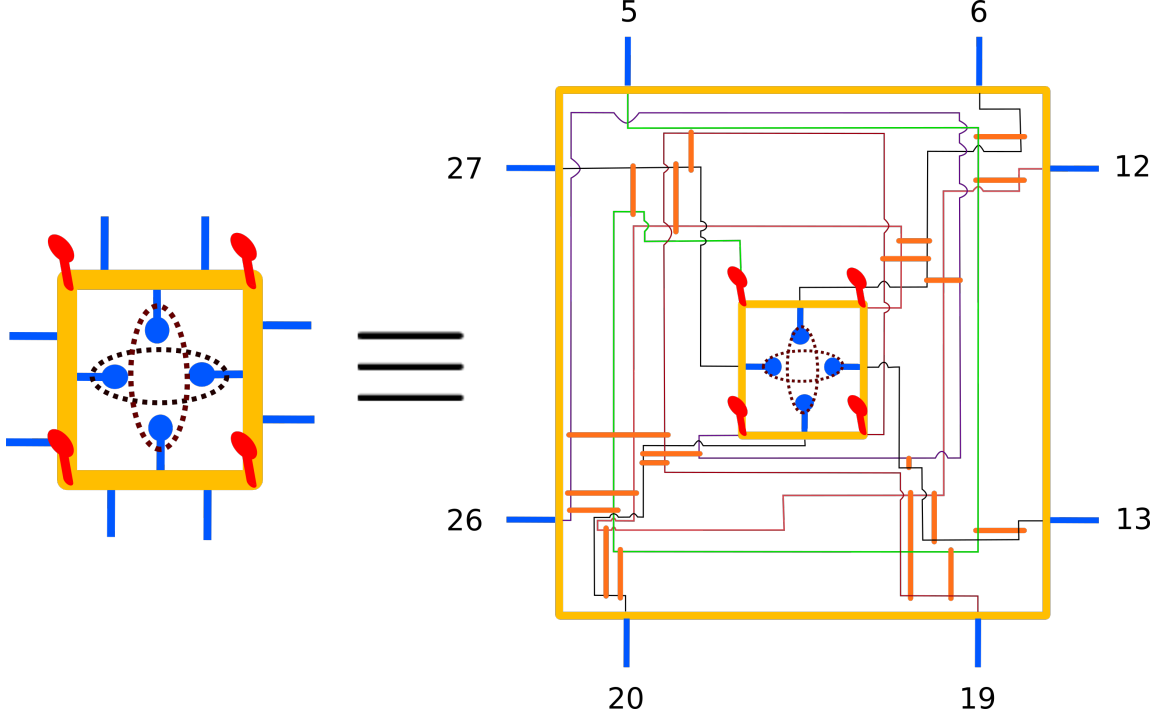
Figure 10. Decomposition of nonlocal unitary disentangler (yellow block) into arrangement of local two-qubit/pseudospin disentanglers (orange blocks). The green, pink, brown and violet lines represents the Hilbert space for pseudospins labelled 5, 12, 19 and 26 respectively. The orange block operates on the lines crossing its edges.

We now construct an auxillary state $|\rho\rangle$ by extracting the two pseudospin configuration of α, β and the state $|\Psi_{(j-1)}\rangle$, and embedding it into a higher dimensional Hilbert space that constitutes all the subsystem states $|\Phi_{(j)}^n\rangle$. If $n'_{max} > n_{max}$, then the states $|\Phi_{(j)}^n\rangle$ are augmented by the states $|\chi_{n_{max}+1}\rangle, \ldots, |\chi_{n'_{max}}\rangle$ orthogonal to them. This leads to the following $|\rho\rangle$ for $n'_{max} \leq n_{max}$

$$|\rho\rangle = \sum_{m',n'} D_{\alpha,\beta}^{m',n',(j-1)} |m'\rangle_{\alpha,\beta} |\Phi_{(j)}^{n'}\rangle \ . \tag{3.16}$$

On the other hand, if $n'_{max} \geq n_{max}$,

$$|\rho\rangle = \sum_{m',n'=[1,n_{max}]} D_{\alpha,\beta}^{m',n',(j-1)} |m'\rangle_{\alpha,\beta} |\Phi_{(j)}^{n'}\rangle + \sum_{m',p=[n_{max}+1,n'_{max}]} D_{\alpha,\beta}^{m',p,(j-1)} |m'\rangle_{\alpha,\beta} |\chi_p\rangle \ . \tag{3.17}$$

We now need to find an unitary transformation $U_{\alpha,\beta}$ that maps $|\Psi_{(j)}\rangle$ to $|\rho\rangle$. This can be constructed by first performing Gram-Schmidt orthonormalization to find a state $|\rho_\perp\rangle$ that is orthogonal to $|\Psi_{(j)}\rangle$

$$|\rho^\perp\rangle = \mathcal{N}(|\rho\rangle - |\Psi_{(j)}\rangle\langle\Psi_{(j)}|\rho\rangle) \ , \tag{3.18}$$

where $\mathcal{N}$ is the normalisation factor. The inner product $\langle\Psi_{(j)}|\rho\rangle$ can then be determined from eq.(3.16) and eq.(3.17), allowing us to determine the state $|\rho^\perp\rangle$ exactly. From here,

we can construct the unitary operation

$$U_{\alpha,\beta} = \exp\left(\tau\left(|\rho_\perp\rangle\langle\Psi_{(j)}| - |\Psi_{(j)}\rangle\langle\rho_\perp|\right)\right) \ , \tag{3.19}$$

where the many-body rotation angle is $\tau = \cos^{-1}(\langle\Psi_{(j)}|\rho\rangle)$.

In order to find the next unitary operator in the decomposition, we recast $|\rho\rangle$ in the pseudospin basis of another set of states α', β' (as in eq.(3.15)). A similar representation for $|\Psi_{(j-1)}\rangle$ is found in the pseudospin basis of α', β', following which the steps outlined above are followed once again to obtain the disentangler $U_{\alpha',\beta'}$. In this way, the entire decomposition given by eq.(3.14) is obtained. A quantum circuit description for a particular nonlocal unitary operator $U_{(j)}$ (yellow block in Fig.9) is given in Fig.10. The orange blocks on the right panel of Fig.10 disentangles a pair of pseudospins. The existence of a quantum circuit design of the nonlocal disentangler $U_{(j)}$ as a combination of two local disentanglers justifies a holographic description for MERG [24].

We close this section by providing a comparison between the MERG architecture Figs.9 and 10 and other tensor network methods, e.g., multiscale entanglement renormalization group ansatz (MERA) [19] and deep MERA [71]. The first important difference worth noting is that while each transformation layer in MERG is composed only of unitaries, in MERA and DMERA, every transformation layer is composed of a layer of two-local unitaries and a layer of isometries. Next, both MERA and DMERA involve variational parameters in the transformation layers. On the other hand, MERG does not have variational parameters: the unitary transformations are solely determined via the form of the Hamiltonian that is block diagonalized and the choice of quantum fluctuation energy scale ω (eq.(2.2)). Finally, in MERG and DMERA, each unitary transformation layer is composed of many sublayers of two local unitary disentanglers gates; this is defined as the depth of the unitary gate D. For instance, in DMERA, the depth D is equal to the number of variational parameters employed in the transformation layer. However, in MERG, the depth at each unitary RG step (D_j) is equal to the circuit complexity, i.e., $D_j = UCC_j = 16j - 10$ (Fig.7).

3.4 Emergence of T.O. ground state and quantum error correcting code

The topological ordered ground state manifold of the Mott liquid state $\{|\Gamma_+\rangle, |\Gamma_-\rangle\}$ is characterized by a Wilson loop operator W. In the language of a quantum error correcting code [63], W corresponds to *a stabilizer* that leaves the states invariant upto an overall phase: $W|\Gamma_\pm\rangle = \pm|\Gamma_\pm\rangle$. We can see, therefore, that the MERG program leads to the quantization of the expectation value of the Wilson loop operator, $\langle\Psi_{(j)}|W|\Psi_{(j)}\rangle$, by successfully resolving all quantum fluctuations that can disturb the states $|\Gamma_\pm\rangle$. Fig.11 shows that the Wilson loop expectation value $\langle\Psi_{(j)}|W|\Psi_{(j)}\rangle$ has minimal growth in the first few RG steps, followed by a sharp rise between the second last and final RG steps, ending at $\langle\Psi_{(j^*)}|W|\Psi_{(j^*)}\rangle = 1$. This shows that in the state $|\Gamma_+\rangle$, the pseudospins form a pair of maximally entangled singlets that are distilled out from a (bare) state where the entanglement is initially spread among many members. For example, in the second last RG step, there are $CC(2) = 22$ entangled bonds compared to just the two singlet bonds in $|\Gamma_+\rangle$. This explains the sharp distillation of topological order via the URG procedure.
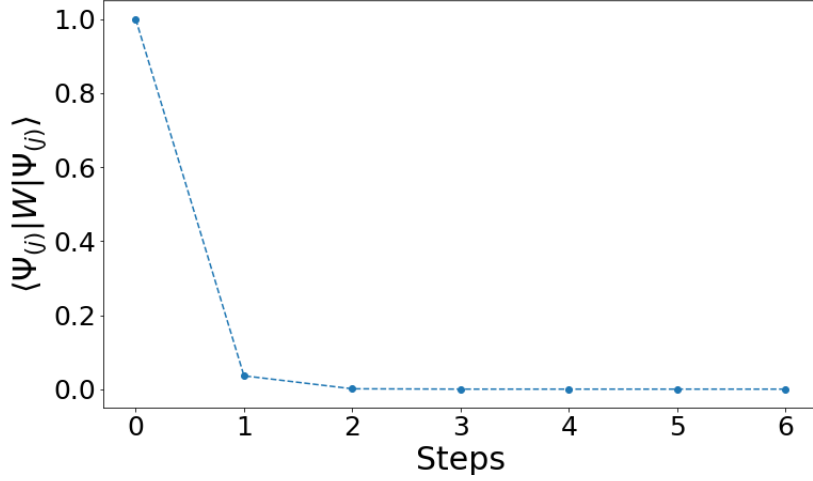
Figure 11. Evolution of the expectation value of the Wilson loop along the RG trajectory.

In the language of topological quantum error correcting codes, the the topologically ordered states form the *codewords*, and the unitaries U_j of the URG *decode* them. On the other hand, the reverse unitaries $U_j^\dagger$'s of the MERG sequentially *encode* the codeword $|\Gamma_+\rangle$ in a higher dimensional Hilbert space by re-entangling them with the decoupled degrees of freedom (Fig. 3). The identity $U_j U_j^\dagger = 1$ describes the encoding-decoding program. An example state obtained by the encoding step: $U_{j^*+1}^\dagger |\Psi_{j^*}\rangle = |\Psi_{j^*+1}\rangle$ is represented in Fig.6. The decoding strategy $U_{(j)}|\Psi_{(j)}\rangle = |\Psi_{(j-1)}\rangle$ (forward RG) leads to the *stabilizer* qubits (disentangled pseudospins) which can maintain a non-trivial error syndrome in the presence of external noise in the encoded state $|\Psi_{(j)}\rangle$. In this way, MERG can generate an encoding-decoding program using the form for U (eq.(2.2)) for the case of a parametric noise that can be modelled into a Hamiltonian H_1 different from H (eq.(2.1)). Thus, MERG is realized as a quantum error correction code that resolves the internal quantum fluctuations, leading to a topological codeword manifold [67]. Further, this platform paves the way for optimal error correction strategies in cases of more general environmental noise. In the next section, we will track the many-body entanglement features along the RG flow that leads to the topological ordered state.

4   Entanglement RG flow towards the topologically ordered ground state

The entanglement features [81] of a many-body state are formed by a collection of various quantifiers, e.g., mutual information, entanglement entropy, Renyi entropy, purity etc. for the Schmidt (entanglement) spectra obtained for all possible different biparititions. In the present context, the topologically ordered state [94] is characterized by emergence of (real space) short ranged strongly entangled singlet pairs (similar to the short ranged resonating valence bonds (RVB) [95]) in the low energy subspace. For example, in the Mott liquid ground state wavefunction eq.(3.1), the members of the pairs (6,20) and (13,27) (Fig.4) are

maximally entangled and belong to different sides of the $E_F = 0$ energy boundary (FS); the large k-space separation ensures that these are short ranged pairs in real space. In this section, we investigate the RG crossover into a system of strongly entangled pairs $|\Gamma_+\rangle$ amidst scattering between all pseudospin pairs by tracking a subset of their *entanglement features*.

4.1 Definitions and Computation method

We first define the entanglement features that has been used for the analysis.

1. *Mutual information(MI)* between a pair of pseudospins characterizes the *strength of entanglement* [24, 39] among the members i and j

$$I(i:j) = -Tr(\rho_i \ln \rho_i) - Tr(\rho_j \ln \rho_j) + Tr(\rho_{ij} \ln \rho_{ij}) \;, \tag{4.1}$$

where ρ_i,ρ_j are the 1-pseudospin reduced density matrices (RDM) and ρ_{ij} is the 2-pseudospin RDM. More precisely, if pseudospins (i,j) are individually strongly entangled with the rest of the pseudospins, then ρ_{ij} has a huge spread in its probability eigenvalues. This lowers the MI content among (i,j) and characterizes a weakly entangled pair. On the other hand, if the pseudospins are strongly entangled as a pair, then ρ_{ij} has a smaller spread and characterizes a strongly entangled pair. For example, the singlet pair $(i,j) = (6,20)$ in eq.(3.1) has maximum possible mutual information $I(i:j) = 2\ln 2$, and clearly $\rho_{ij} = 1$ is a pure state with zero spread.

2. *Information distance* is a distance measure between pseudospins computed as the negative logarithm of the MI

$$d(i,j) = -\ln \frac{I(i:j)}{2\ln 2} \;. \tag{4.2}$$

$d(i,j)$ is defined such that strongly entangled pairs have smaller information distance. The maximally entangled pairs $(6,20)$ in $|\Gamma_+\rangle$ has zero information distance $d(6,20) = 0$, while the pair of disentangled pseudospins $(1,2)$ has $d(1,2) \to \infty$. In a many-body state, $|\Psi\rangle$ is the collection of all possible information distances $d(i,j)$, and describes an effective *spacetime geometry* [24]. This provides a link between the quantum circuit network descriptions of state $|\Psi_{(j)}\rangle$ and the entanglement spacetime geometries $d(i,j)'s$ obtained at each RG step. In this way, the strongest entangled members in the state $|\Psi_{(j)}\rangle$ characterizes the *geodesic-* $d_g = \min_{i,j} d(i,j)$ of the spacetime geometry.

3. *Purity* is defined as $Tr(\rho^2)$, and characterizes the spread in the probability eigenvalues of the RDM. Purity is useful for classifying the amount of entanglement information lost in obtaining the RDM, i.e., the partial tracing over the rest of the entangled degrees of freedom.

4. The *Schmidt spectrum*/entanglement spectrum [96] is a set of numbers $\{\lambda_i\}$ obtained from a Schmidt decomposition of $|\Psi\rangle$ across a bipartition, e.g., between 2 and $N-2$ pseudospins

$$|\Psi\rangle = \sum_{i=1}^{k} \lambda_i |\phi_i\rangle_2 |\Phi_i\rangle_{N-2} \;, \tag{4.3}$$

where $|\phi_i\rangle$ are the mutually orthogonal two-pseudospin states and $|\Phi_i\rangle$ are the orthogonal many-body configurations of the $N-2$ pseudospins. For such a bipartition of 2 and $N-2$ pseudospins, the quantity k is given by $k < min(d_A, d_B) = 4$, where d_A, d_B are the subsystem Hilbert space dimensions.

5. The *Physical distance* $d_p(i, j)$ between pseudospin pairs in momentum space is obtained by first computing the k-space distance using the Euclidean metric

$$d(\mathbf{k}_i, \mathbf{k}_j) = \sqrt{(k_{ix} - k_{jx})^2 + (k_{iy} - k_{1y})^2} \ , \tag{4.4}$$

and then inverting $d(\mathbf{k}_i, \mathbf{k}_j)$ to obtain the relation $d(i, j) = 1/d(\mathbf{k}_i, \mathbf{k}_j)$.

The computation method we apply is as follows. We first apply the MERG technique on the state $|\Psi^*\rangle$ to obtain all the states $|\Psi_{(j)}\rangle$ in the steps outlined in Fig.3. This is followed by a computation of the one- particle and two-particle Schmidt spectra (as in eq.(4.3)) for all possible pairs of pseudospins. The various entanglement features listed above can then be computed numerically from the Schmidt spectra.

4.2 Results on emergence of strongly entangled short distance pairs

In Fig.12 (left panel), we present the decrement of the geodesic distance d_g ($d_g \to 0$) under RG flow across the EHM network (Fig.9). This signals the emergence of strongly entangled pairs with high MI content $I_{max}(i : j) = 2\ln 2$ and $d_g = 0$) at the low energy stable fixed point of the RG. Complementary insight is obtained in the right-hand panel of Fig.12, which shows the concomitant reduction in real-space physical distance d_p between the strongest entangled pseudospins. We have also labelled the pairs carrying the highest MI at each RG step. Initially, the pseudospin pair $(24, 17)$ lying to one side of the FS (see Fig.4) and connected by tangential scattering vertex L, carry the highest MI and comprise the geodesic $d_g = 1.66$, while the d_p between them is 4 lattice spacings. However, beyond the second RG step, the system undergoes a crossover into a phase comprised of high MI pseudospin pairs $(17, 3)$, $(18, 4)$ etc. connected via backscattering vertex (K vertex). The pair $(17, 3)$ is formed by states belonging to opposite side of the FS: the physical distance between these pairs has thus shrunk to $d_p = 1$ lattice spacing. In this way, we observe the emergence of $d_p = 1, d_g = 0$ (short distance) strongly entangled pairs $(6, 20)$, $(13, 27)$ amidst competition among various entangled pairs connected via forward scattering (V vertex), backscattering and tangential scattering. Additionally, we note that the emergence of such pairs is correlated with the quantization of the Wilson loop expectation value signalling the onset of T.O. (Fig.11).

Fig.13 shows the MERG analysis of the MI content of the following pairs: $(13, 27)$-connected via backscattering (K), $(20, 27)$-connected via tangential scattering (L) and $(13, 12)$-connected via forward scattering (V). The analysis reveals that, starting from the third RG step, $I(13 : 27)$ dominates over that of the other two. This again substantiates the emergence of strongly entangled pairs $(13, 27)$ and $(6, 20)$ in the bulk of EHM, and is a direct outcome of the RG relevant backscattering vertex (K) together with irrelevant forward (V) and tangential (L) scattering vertices (see eq.(3.8) and discussion below). Finally, we track the RG contribution of the 1-pseudospin and 2-pseudospin Schmidt spectra in quantifying the
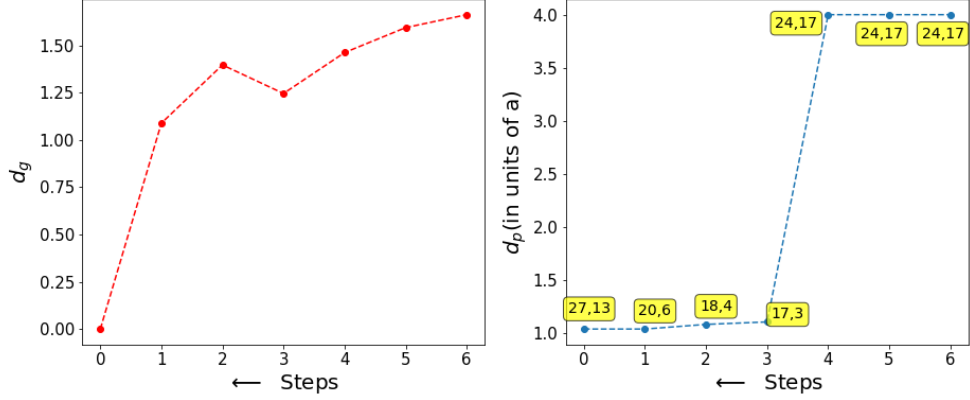
Figure 12. Left Panel: Scaling of the information geodesic d_g. Right Panel: Scaling of the corresponding physical distance d_p between the strongest entangled pseudospin pairs.
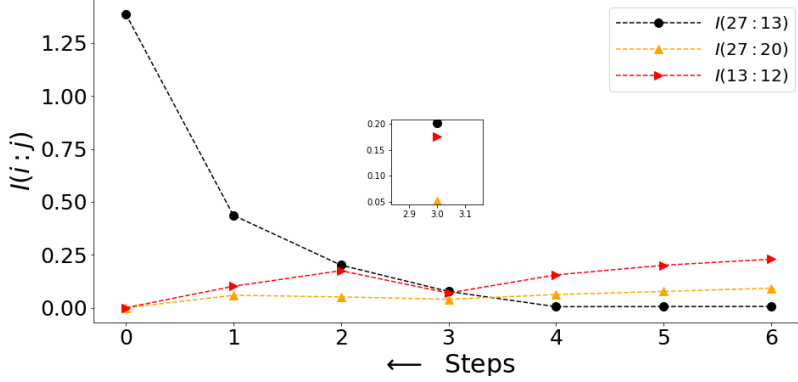

Figure 13. Variation of Mutual information (MI) $I(i : j)$ for pseudospin pairs connected via tangential scattering (pair $(27, 20)$), forward scattering (pair $(13, 12)$) and backward scattering (pair:$27 : 13$) processes. Inset shows the MI values at the third RG step.

growth of MI for the pair $(13, 27)$. The left panel of Figure 14 represents the RG flow for the Schmidt spectra $\{\lambda_{13}\}, \{\lambda_{27}\}$ of pseudospins 13 and 27. The plot clearly shows that both pseudospins follow an (almost) identical pattern: the distance between the two eigenvalues of, say, $\{\lambda_{13}\}$ initially grows under the RG till the third step, then showing a dramatic collapse towards a degeneracy at the fixed point. The orange and green curve in the right panel represents the purity of the respective RDMs ($Tr(\rho_{13}^2)$ and $Tr(\rho_{27}^2)$). Both purities display the crossover of the spread in probability eigenvalues from low to high, leading to increase in their individual entropies. Further, the purity of the pair of the pseudospins $Tr(\rho_{27,13}^2)$ increases eventually to 1, corresponding to a decrease in the joint entropy for these two pairs of pseudospins: $-Tr(\rho_{27,13} \ln \rho_{27,13})$. Taken together, the increase in individual entropies and the decrease in joint entropy signals the increase in the MI of the individual pseudospins. This is another way in which we witness the isolation of strongly
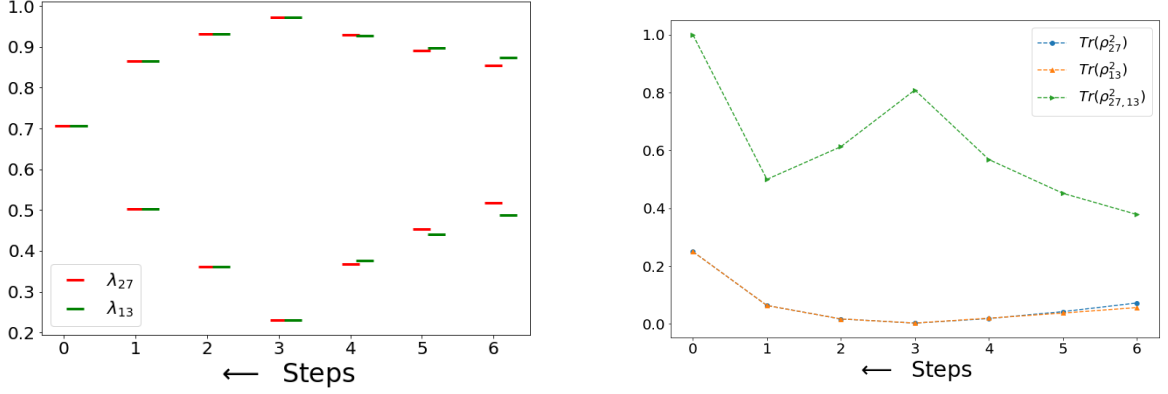
Figure 14. Left Panel: Schmidt spectrum renormalization for the pseudospin pair $(27, 13)$. Right Panel: Purity for the one- and two- pseudospin reduced density matrix.
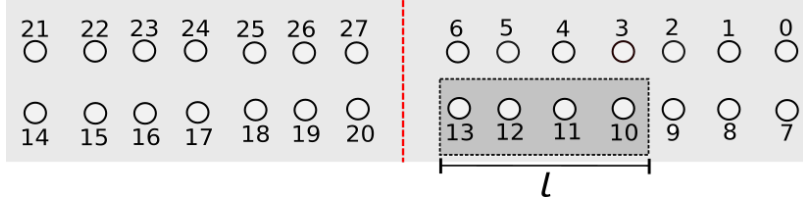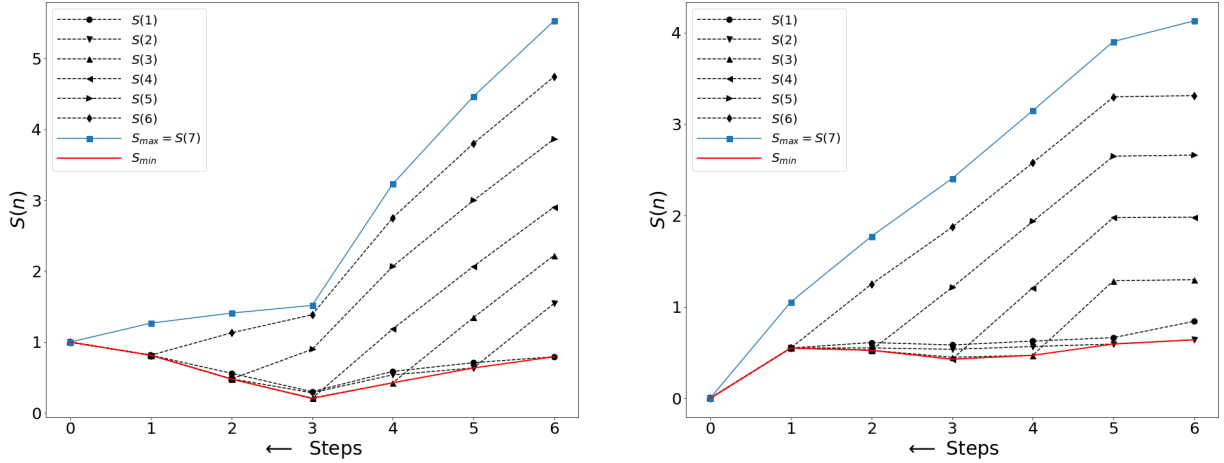

Figure 15. Momentum space partitioning (red dotted line) across blocks belonging to opposite sides of the Fermi surface. l is the block size.

entangled pseudospin pairs from the rest in the bulk of the EHM.

Thus, the nature of RG flow equations at a given quantum fluctuation energy scale ω can be seen to dictate the *entanglement geometry* content of the EHM network leading to the T.O. ground state. In the next subsection, we discuss the RG evolution of the entanglement geometry, information entropy content and the distinct nature between the gapless and gapped states it give rise to.

4.3 Distinct scaling features of block entanglement entropy and entanglement geometry for the T.O. and normal metal phase

We compute here the entanglement entropy across a partition in momentum space. As shown in Fig.15), we construct momentum space blocks of increasing lengths (l) on one side of the FS, with the dark/light grey regions being the two members of the partition. For the Mott liquid state, the RG flow of the entanglement entropy (EE, in units of $\ln 2$) in shown in the left panel of Fig.16. The figure shows an initial decrease of EE with different block sizes (ranging from $l = 7$ to 1), followed by an increase from the third step to the final value of $EE^* = \log 2$ at the fixed point. As presented earlier, this gradual crossover of EE is manifested by the proliferation of strongly entangled (short distance) pairs formed via pseudospin backscattering across the FS. Importantly, we note that at the fixed point, the entanglement entropy $EE^* = \log 2$ is independent of subsystem sizes greater than
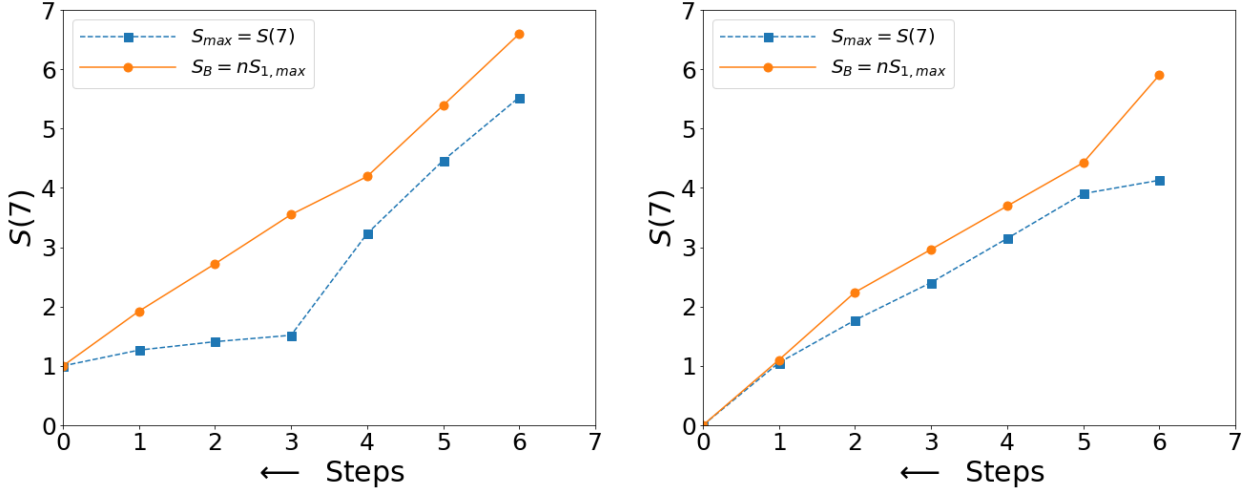
Figure 16. Entanglement entropy (EE) renormalization across the EHM for momentum space partition block sizes 1-7 on one side of FS for Mott liquid (left panel) and for normal phase (right panel).

the momentum space shell width, characterizing the perfect disentanglement of the states outside the emergent space. This clearly suggests a *topological* origin of this entanglement entropy. We also carry out a reverse MERG construction (Fig. 3) for the many-body states in the normal metallic phase for $W > W/2 - \omega > W/2$ of the phase diagram Fig.2. For this, we start from the ground state eq.(B.2) shown in Appendix B. In this case, the EE in right panel of Fig.16 is seen to decrease for various block sizes along the RG flow such that at the RG fixed point, $EE = 0$. This is consistent with the fact that the state eq.(B.2) is separable in terms of momentum space pseudospins. The distinct nature of EE RG flows across the EHM for the gapped T.O and gapless metallic states describes a entanglement phase transition in going from the normal metal phase at $\omega = -W/2$ to Mott insulating phase at $\omega = W/2$.

In order to investigate further the holographic features of the EHMs constructed for the insulating and metallic ground states, we identify at every RG step the causal cone (dashed red line in Fig.9) that extends across the bulk of the EHM for a given block of the EHM boundary (grey shaded area in Fig.9). For the block of boundary pseudospins $7 - 13$ in Fig.9, we first compute the maximum single-pseudospin entanglement entropy ($S_{1,max}$). We recall that the Ryu-Takayanagi formula [3] was shown to hold for MERA [19, 22] and EHM [24] respectively, such that at any given RG step we expect

$$S(7) \leq n \, S_{1,max} \,, \tag{4.5}$$

where n corresponds to the perimeter of the causal cone/minimal surface at that RG step, i.e., the number of links that must be cut in order to isolate the boundary block of length 7. Indeed, we find in Fig.17 that the above relation is satisfied by both the Mott insulating and normal metallic ground states. Importantly, we find that the quantity $S_{1,max}$ arises from

Figure 17. Blue curve: Entanglement entropy (EE) renormalization across the EHM for momentum space partition block size 7 on one side of FS for Mott liquid (left panel) and for normal phase (right panel). Orange curve: Renormalisation of the entanglement entropy bound obtained from the causal cone/minimal surface of block size 7 for Mott liquid (left panel) and for normal phase (right panel).

the entanglement of the pseudospin 13 with all the other pseudospins $(7 - 12)$. Pseudospin 13 resides deep in the IR, i.e., proximate to the Fermi surface of the normal phase, and a member of the singlet pair $(13, 27)$ that is part of the topologically ordered insulating ground state. This shows that the last link that is cut by the causal cone deep within the IR corresponds to the degrees of freedom proximate to the nodal Fermi surface (of the 2D tight-binding problem on the square lattice). For the metallic ground state, this reflects the holography arising from the Fermi surface [5]. On the other hand, for the insulator ground state, the causal cone is a holographic witness to the emergence of the nonlocal Wilson loop (eq.(2.8), see also Fig.11)) at the IR fixed point.

The entanglement phase transition between the two phases can also be seen from the contrasting entanglement geometry evolution across the EHM for the two ground states. The left panel of Fig.18 shows the RG evolution of information distances d_{ij} in the Mott insulating regime, while the right panel of Fig.18 shows the evolution of inverse information distances $1/d_{ij}$ in the marginal Fermi liquid metal. The blue curve (D and $1/D$ in the two figures) tracks the RG evolution of the largest information distance (minimal MI pair) in the emergent space geometry. The red curve (d_g and $1/d_g$ in the two figures) tracks the geodesic, while the black dots represents the information distances between various (i, j) pairs. The increase of MI in the emergent window of the Mott liquid is described by a shrinking space, i.e., $D - d_g$ reduces under RG flow towards the stable fixed point where all distances collapse to zero. On the other hand, the decrease of MI in the normal metal is described by an expanding space as both $d_g, D \to \infty$ under the RG flow. It is important to note that the information distance $d(a, b)$ in the IR limit is related to the negative logarithm
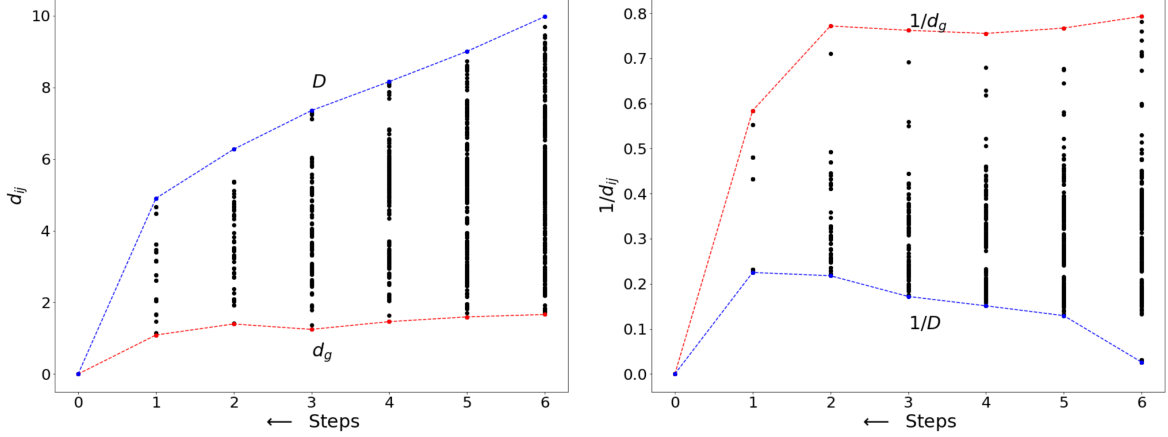
Figure 18. Evolution of the information distances between various pseudospin pairs across the EHM for the normal state (right panel) and Mott insulating state (left panel). D and d_g are the largest and smallest (i.e., geodesic) information distances respectively.

of the two pseudospin (i.e., two electron-two hole) Green's function in momentum space [24]

$$d(a,b) \sim -\log G(a,b) = -\log(\langle \Psi_{(j)}|A_a^+ A_b^-|\Psi_{(j)}\rangle) \ , \tag{4.6}$$

where A_a^+ and A_b^- are pseudospin raising/lowering operators. Recall that in the Mott insulating phase Fig.12 (also the lower boundary in Fig.18 left panel), the information geodesic $d_g(a,b)$ is related to the nodal pair $(13, 27)$ that forms the singlet at the IR fixed point in the bulk of the EHM. Following Lee and Qi [24], we note that in our case the information geodesic at the IR fixed point is given by

$$d_g(13, 27) = -\log \exp(-\xi|2k_F|) = \xi|2k_F| \ , \tag{4.7}$$

where ξ is the real-space correlation length between the constituents of the Mott pseudospin singlets eq.3.1. This indicates the equivalence between the correlator deep in the EHM and the the 4-particle Green's function proximate to the Fermi surface. Similarly, in the EHM constructed for the metallic ground state, the divergence of $d_g = -\lim_{k \to k_F} \ln(|k - k_F|)$ is tied to the RG scaling of the entanglement towards the gapless Fermi surface [5].

We summarise by noting that the entanglement features and geometry of the EHM for the topologically distinct insulating and metallic phases we are studying here are markedly different: the former (T.O. phase) is marked by a nontrivial $EE = \log 2$ and vanishing d_g, while the latter (normal phase) is characterised by $EE = 0$ and a diverging d_g. This confirms that our EHM network carries important information with regards to the topological nature of a many-body state, and can sense a transition between the two phases through their entanglement features. In the next section, we will quantify this information flow across the EHM network using measures from information theory and deep learning (DL). We will thus show the equivalence between our MERG based EHM and a deep neural network (DNN) architecture.

5 A Deep Neural Network based on EHM

A deep neural network (DNN) [72] is a sequence of layers of mathematical operations that transform an input feature vector X into $\hat{X}$ while keeping only the essential parts relevant to the target output vector Y. An optimal $\hat{X}$ can be obtained via Lagrangian minimization [76]

$$\mathcal{L}[p(\hat{x}|x)] = \mathcal{I}(X:\hat{X}) - \beta\mathcal{I}(\hat{X}:Y) , \tag{5.1}$$

where the *mutual information like quantity* $R = \mathcal{I}(\hat{X}:X)$ quantifies the complexity of the representation, and $\mathcal{I}_Y = \mathcal{I}(\hat{X}:Y)$ is the amount of information relevant to Y preserved in $\hat{X}$. The quantity β is the tradeoff parameter, while the function $p(\hat{x}|x)$ is the conditional probability. An optimal representation $\hat{X}$ is one for which the MI (R) is reduced and $\mathcal{I}_Y$ is preserved. This is known as the information bottleneck (IB) principle [76]. A DNN following the IB principle can be considered optimal. In the section below, we will demonstrate that EHM based MERG fulfills the IB principle, and is therefore on par with a optimally functioning supervised DNN.

5.1 Demonstrating the IB principle for EHM based on MERG

We have seen earlier that the MERG is a family of unitary disentanglement transformations with an input many-body eigenstate (Fig.3), leading to simpler representations with a lower number of entangled qubits. It was also demonstrated that the EHM of Fig.9 is a tensor network representation of MERG. An important question to ask in this regard is: *does the EHM network architecture naturally follow the IB principle?*

In order to perform the information bottleneck analysis, we first prepare the entanglement RG results as a data model. Every pair of qubits in the many-body state can be labelled as (a,b). With every pair (a,b) is associated one *feature*: $F(a,b) = I(a:b)$ (the MI defined in eq.(4.1)). The larger the MI, the stronger is the entanglement within the pair. Next, we perform a classification of all pairs into two classes, strongly and weakly entangled, by using a *classifier* $C(a,b)$

$$C(a,b) = \begin{cases} 0 & 0 \le F(a,b) < \log 2 \\ 1 & \log 2 \le F(a,b) \le 2\log 2 . \end{cases} \tag{5.2}$$

In order to compute the set $(R, \mathcal{I}_y)$ at each step of the RG, we first prepare the input vector (X), RG transformed vectors $\hat{X}$ and target vector Y. The input feature vector $X = \{F(a,b)\}$ is built from the state $|\Psi_{(6)}\rangle$, constituted of MI values for $\binom{4}{2} = 6$ pairs (a,b) made of 4 pseudospin qubits (6, 13, 20, 27). S is a list of these pairs, where S_i is the ith element in the list

$$S = \{(13,6), (20,6), (27,6), (20,13), (27,13), (27,20)\} \tag{5.3}$$

Note that the above four qubits (Fig.4) have been chosen so as to eventually compose the emergent subspace at the RG fixed point, and therefore constitute the entanglement features of the T.O. ground state. We similarly construct the transformed feature vector $\hat{X}_j$ from $|\Psi_{(j)}\rangle$ at each RG step. The target vector $Y = \{C(a,b)\}$ is constructed for pairs eq.(5.3)
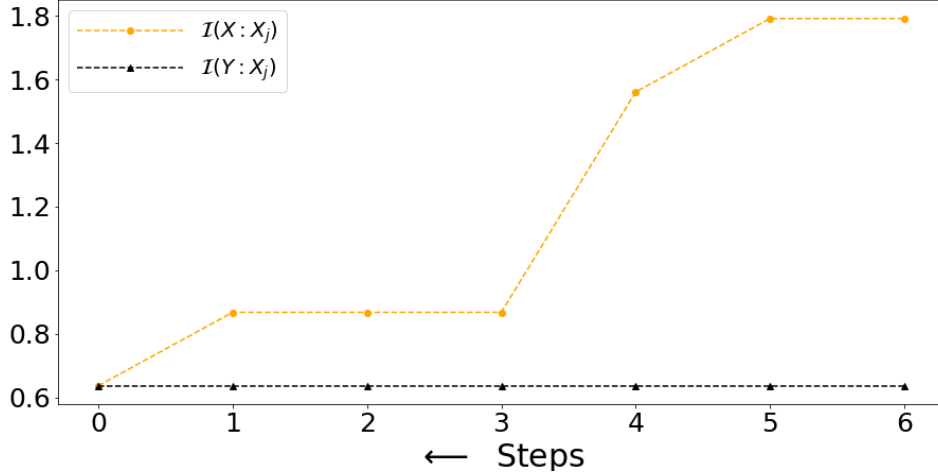
Figure 19.   Testing the information bottleneck principle for EHM network. Orange curve represents the representation complexity $R = \mathcal{I}(\hat{X}_j : X)$, while black curve represents $\mathcal{I}_Y = \mathcal{I}(Y : \hat{X}_j)$, the information about class Y present in the representation.

in S using the state $|\Gamma_+\rangle$ at the fixed point eq.(3.1). From these datasets, we compute the information plane coordinates [76, 97] $R = \mathcal{I}(\hat{X}_j : X)$ and $\mathcal{I}_Y = \mathcal{I}(Y : \hat{X}_j)$.

The representational complexity R (orange curve) displayed in Fig.19 is seen to decrease across the EHM, while the mutual information I_Y (eq.(4.1), black curve) is constant throughout at a value of 0.636. This demonstrates clearly that the IB principle is met by the MERG based EHM. This allows us to make the following mapping between the MERG based EHM and a DNN: the disentanglement transformations (yellow blocks in Fig.9) are equivalent to the *hidden layers* of a DNN that outputs simpler representations. A constant value of I_Y across the EHM suggests a strong dependence between Y and representation $\hat{X}_j$ obtained at various RG transformation steps. Fig.20 verifies the strong dependence between the representation of MI values $\hat{X}_j$ (Figs. 20 (a-e)) at each RG step and the class Y (Fig.20(f)). We observe that the MI values for the pairs $(6, 13)$ and $(20, 27)$ either belong simultaneously to the strongly entangled class $C(6, 20) = C(13, 27) = 1$, or to the weakly entangled class $C(6, 20) = C(13, 27) = 0$. This results in the preservation of mutual information $\mathcal{I}(Y : \hat{X}_j)$ at every RG step (black line in Fig.19).

5.2   Constructing a DNN model for classifying *entangledness* of a pair

Given the demonstration of the IB principle for the EHM based on MERG, we construct a conditional probability DNN model for predicting the eventual fate of a given pair (a, b) to be either strongly $(C(a, b) = 1)$ or weakly entangled $(C(a, b) = 0)$. This is done in the following way: given any pair (a, b) and its feature $F(a, b)$ at each RG step j, we compute the conditional probability $P(C = 1|F(a, b))$ by performing a statistical analysis of the MI dataset. Below we list the specifics of the MERG based DNN model:

1. The bare representation X_6 is constructed from initial state $|\Psi_{(6)}\rangle$ by collecting the
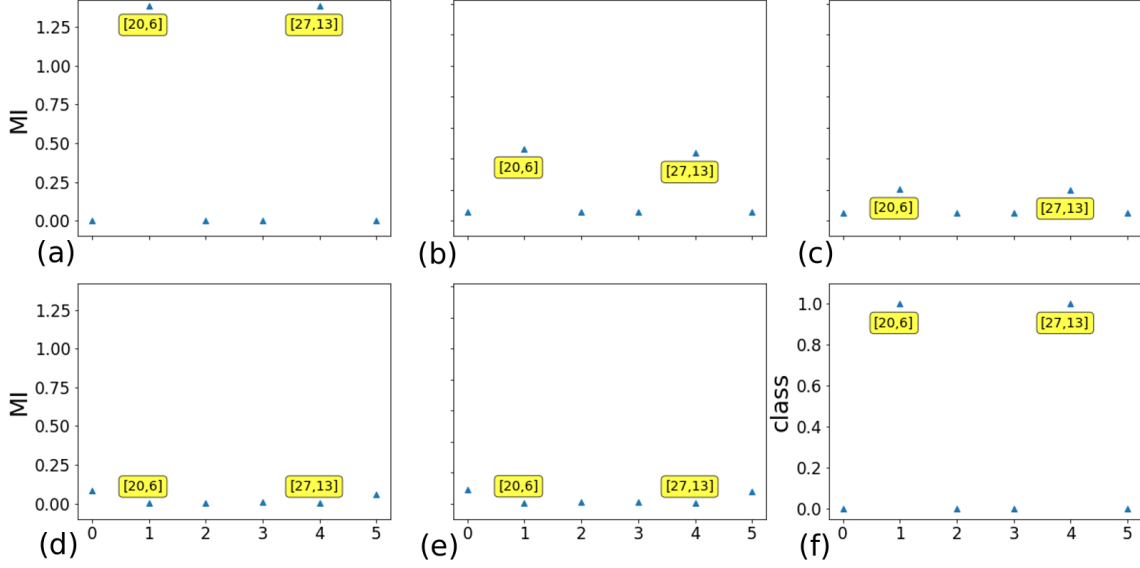
Figure 20. (a-e) MI values $\hat{X}_j$ of the list of pairs S for states $|\Gamma_+\rangle$, $|\Psi_1\rangle$, $|\Psi_3\rangle$, $|\Psi_4\rangle$, $|\Psi_6\rangle$. (f) Class Y for the pairs in $|\Gamma_+\rangle$.

MI values of all $\binom{28}{2} = 378$ (a, b) pairs.

2. Unitary transformations equivalent to *hidden layers* are linear maps that act on the state $|\Psi_{(6)}\rangle$, followed by state $|\Psi_{(5)}\rangle = U_6|\Psi_{(6)}\rangle$ and so on. This is in contrast with standard deep learning, where nonlinear filters and weight matrices are chosen variationally in constructing the transformation layers [98]. In our formalism, the unitary operators are constructed exactly (see Sec.2.2). Furthermore, because of the exact nature of the construction, there is no requirement of a training dataset for the construction of the DNN.

3. From each of the many-body states, we compute the MI values (eq.(4.1)) using one- and two-pseudospin Schmidt spectra (eq.(4.3)). The collection of 378 MI values at each RG step j is referred to as the bottlenecked representation (X_j) of X_6.

4. At each RG step j, we compute the joint probability $P(F(a,b), C(a,b))$ between the bottlenecked representation X_j and the target classifier $\hat{Y}$. From this, we compute the conditional probability for the eventual fate at $j^* = 0$ of the *entangledness* of a pair given its MI value at RG step j.

We now set the criterion for a DNN model ideal from our perspective: such a DNN should predict that in the bulk of the EHM, the pairs $(13, 27)$ and $(6, 20)$ are strongly entangled$(C = 1)$ while all others are weakly entangled ($C = 0$), as observed from the state $|\Gamma_+\rangle$ (eq.(3.1)). Note that we have already shown via entanglement RG that the formation

of strongly entangled short distance pairs demonstrates the onset of T.O. (Sec.4.2). Therefore, if the DNN model correctly predicts the eventual fate of the pairs, it is then equivalent to predicting the onset of T.O.

Fig.21 shows that the conditional probability $P(C = 1|F(a, b))$ for the pairs $(6, 20)$ and $(13, 27)$ to be strong $(C = 1)$ are small to start with during the RG flow; however, after the third unitary RG step, it rises to value 1. On the other hand, the conditional probability vanishes for two other pairs $(20, 4)$ and $(24, 17)$. In this way, we demonstrate that layers near the UV scale of the EHM network are *holographic witnesses* to the emergence of T.O. at the IR scale. The existence of such holographic witnesses is further demonstrated in Fig.22 by the prediction of the eventual histogram distribution of MI from the initial layers of the EHM. Specifically, Fig.22(a-c) is the MI histogram distribution among pairs in S (formed from the pseudospins 6,13,20,27) and predicted from the zeroth, second and third unitary transformation layers of the EHM network. We find that the MI distribution predicted after only 3 layers already matches with that obtained after 6 layers Fig.22(d). This prediction process is further validated via a null hypothesis test: can the MI distribution of a random tensor network simulate the predicted MI distribution of the target? The statistical distance histogram displayed in Fig.23 shows that there is only 4% probability for the predicted MI distribution to be obtained from a random tensor network. This proves the uniqueness of the target tensor network obtained from the DNN.

Finally, we demonstrate two example cases to check the DNN's ability to distinguishing a metal from a insulator. For this, we compute the mutual information content $\mathcal{I}(X_j, X_{j,U=2})$ between the target vector Y, obtained from the final RG step for the case of strong repulsion $U_0 = 8$, and feature vectors $X_{j,U=2}$ obtained at each step for a case of weak repulsion $U_0 = 2$. The red curve in Fig.24 represents $\mathcal{I}(Y : X_{j,U=2})$, showing saturation at a finite value $\mathcal{I}(X_j : X_{j,U=2}) = 0.636$. We note that this is equal to the saturation value between the mutual information of the representation and class $\mathcal{I}(X_j : Y)$ obtained for the case of strong repulsion $U_0 = 8$ (seen as the value of the MI (black curve) in Fig.19). This precise match of results implies that the constructed DNN is able to predict that, even at weak repulsion $(U_0 = 2)$ and low quantum fluctuation scales $(4 - \omega = 0)$, the phase is a Mott insulator. On the other hand, the green curve in Fig.24 is obtained from the mutual information between the MI distribution of a metal $(U_0 = 8, \omega = 8)$ and the target distribution of a insulator. It shows a final sharp dip to the value $\mathcal{I}(X_{j,metal} : Y) = 0$, implying that the gapless phase is not an insulator. This allows us to conclude that the DNN (constructed from the MERG based EHM) can successfully distinguish between RG flows that lead to a gapless metal and a gapped topological insulator. Such a DNN can, therefore, be employed for characterising the metal-insulator transition between the two phases.

6   Conclusions and discussions

In summary, we have demonstrated that MERG flow can be used to track the emergence of a topologically ordered (T.O.), gapped insulating state at low energies in the 2D Hubbard model at 1/2-filling [44, 87]. Upon obtaining the T.O. ground state wavefunction at the
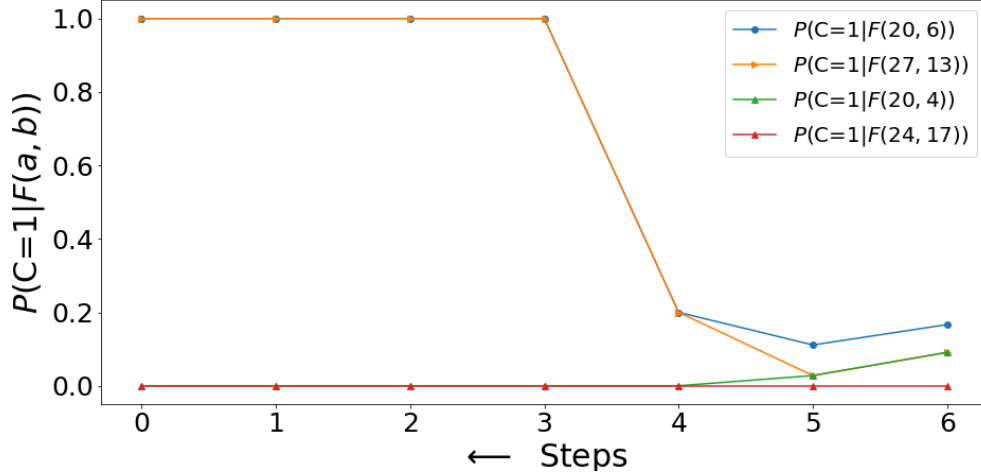
Figure 21. Predicting the eventual entanglement strength (either strong or weak) of a subset of pairs after each RG step using conditional probability.

Mott insulator fixed point of Ref.[44], we perform the inverse unitary transformations to re-entangle the emergent T.O. state with the decoupled degrees of freedom. The fixed point ground state, and the intermediate states reconstructed therefrom, are shown to have quantum circuit representations. In this way, we obtain the tensor network RG equivalent to MERG, called the entanglement holographic mapping (EHM). Each layer of the EHM is shown to be composed of two-local unitary disentanglers, and has a finite depth quantified by the circuit complexity. We show that MERG functions as a topological quantum error correcting code, leading to quantization of a nonlocal Wilson loop characterising the T.O. Mott insulating fixed point deep in the bulk of the EHM. It does so by resolving exactly the quantum fluctuations intrinsic to the system. The robustness of MERG quantum error correcting code against external quantum fluctuations is left for future study.

We have also computed the mutual information for all pseudospin pairs at each RG step, thereby extracting the entanglement geometry content from the EHM. Both the geodesic of the emergent geometry and the physical distance between strongest entangled pairs are shown to shrink along the RG direction, finally vanishing at the IR fixed point. In this way, we show that the emergence of short ranged strongly entangled pairs is concurrent with the emergence of topological order. On the other hand, for the normal metal phase of the 2D Hubbard model, the entanglement geometry is seen to expand and finally approach a separable state in the IR, demonstrating thereby the entanglement content of the EHM in this case is markedly different from that of the T.O. Mott insulating state. We also observe the scaling of momentum space block entanglement entropy (EE) for the metal and T.O. phases. In the T.O. phase the EE displays a nonmonotonic RG flow, i.e., an initial decreases followed by a gradual upsurge to a finite value. Additionally, at the fixed point, the EE is found to be constant for all block sizes. This is in contrast with the monotonic decay of EE in the normal metal phase. Thus, we have realized a concrete example of an
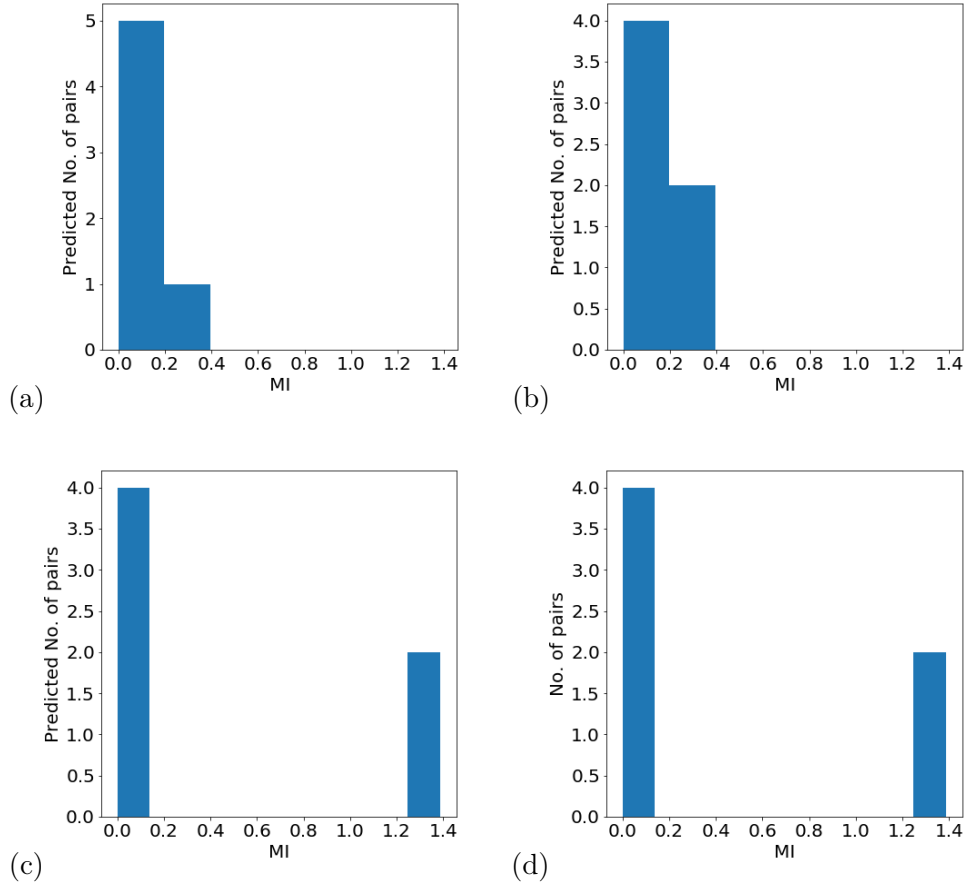
Figure 22. (a-c) Prediction of MI histogram distribution among pairs in list S from conditional probability model after (a) 0, (b) 2 and (c) 3 layers of MERG transformation. (d) MI histogram obtained after 6 layers of MERG transformation.
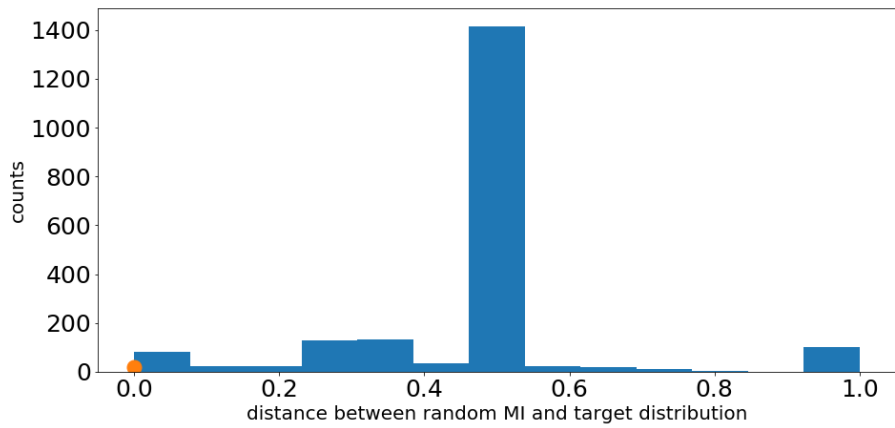
Figure 23. Histogram plot for the statistical distance between MI distribution of a random tensor network and the DNN's predicted MI distribution at the RG fixed point.
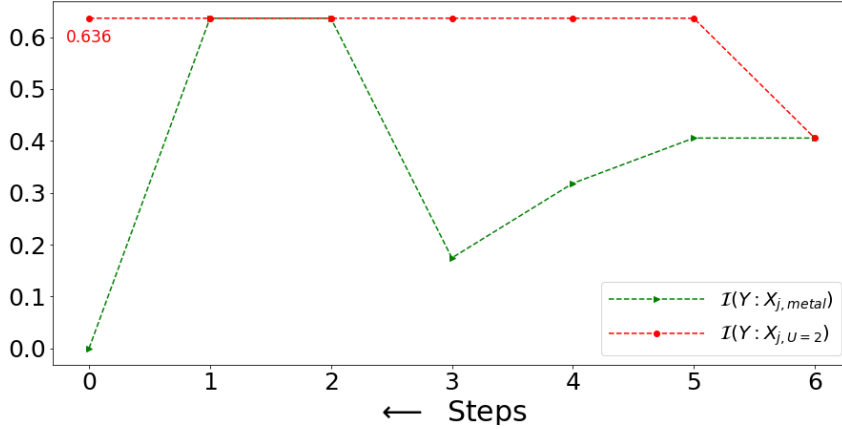
Figure 24. The red curve shows the mutual information content between the MI feature vector of a Mott insulator $X_{j,U=2}$ for $U_0 = 2$, $\omega = 4$ and target vector Y (Mott insulator at $U_0 = 8$, $\omega = 4$. The green curve show the mutual information content between Y and the feature vector of a metal at $U_0 = 8$, $\omega = -4$.

EHM network that is witness to T.O.

Finally, we show that the EHM network functions as an optimal deep neural network (DNN) satisfying the information bottleneck (IB) principle. The unitary transformations lead to successive disentanglement of qubits, naturally reducing the entanglement spread and leading eventually to simpler representations of the many-body state. However, the essential topological content of the IR fixed point is retained across the EHM. The predictive power of the DNN is tested via formulation of the conditional probability model that can classify a given pair to be either strongly or weakly entangled. The model is found to predict the entanglement features in the bulk of the EHM from the layers near its boundary. This is realised by a successful prediction of the onset of T.O. during the RG flow well before the stable fixed point is reached. Further, the DNN is successfully able to distinguish the gapless normal metal ground state from the T.O. gapped insulating state, as well as classify insulating ground states reached at two different values of the Hubbard coupling as belonging to the same class. In this way, the DNN is able to classify different phases of the 2D Hubbard model, as well as distinguish between the RG flows that lead to them. Our work sets the stage for yet deeper investigations of the many-particle entanglement of novel gapped as well as gapless quantum liquids that arise from systems of strongly interacting electrons. It also heralds the development of applications of the MERG formalism for the creation of novel quantum error correcting codes and deep neural network architectures based on the quantum entanglement of many-particle wavefunctions.

Acknowledgments

A   Derivation of the unitary operator

We present briefly the formalism developed in Ref.[44, 87]. H is a Hamiltonian belonging to the space $\mathcal{A}(\mathcal{H}_2^{\otimes N})$, where $\mathcal{H}_2$ is a SU(2) Hilbert space spanned by the generators

$$c_N^\dagger, c_N, \hat{n}_N - 1/2 = c_N^\dagger c_N - 1/2 \ , \tag{A.1}$$

and $\mathcal{A}$ is the antisymmetrizer. We want to find a unitary operation U_N that block diagonalizes the Hamiltonian H in the occupation number space of $N : \{|1_N\rangle, |0_N\rangle\}$

$$(1 - \hat{n}_N)U_N H U_N^\dagger \hat{n}_N = 0 \Rightarrow P_N H (1 - P_N) = 0 \ , \tag{A.2}$$

where $P_N = U_N^\dagger \hat{n}_N U_N$. Using the definition of P_N, we construct the Hamiltonian $H' = P_N H P_N$, leading to the block equation

$$\begin{aligned} P_N H P_N = H' \ &\Rightarrow (P_N H P_N + (1 - P_N)H P_N)P_N = H' P_N \\ &\Rightarrow H P_N = H' P_N \ . \end{aligned} \tag{A.3}$$

It is important to note that

$$P_N H'(1 - P_N) = 0, [H', P_N] = 0 \ , \tag{A.4}$$

implying that the Hamiltonian H' is block diagonal in the rotated basis. A state $|\Psi\rangle$, belonging to the projected space generated by P_N, can be written in the occupation number basis of N

$$|\Psi\rangle = a_1(1 + \eta_N)|1_N \Psi_{1_N}\rangle = a_1|1_N \Psi_{1_N}\rangle + a_0|0_N \Psi_{0_N}\rangle \ , \tag{A.5}$$

where η_N is an (as of now) undetermined operator that connects a many-body state $|1_N \Psi_{1_N}\rangle$ (with N occupied, $|1_N\rangle$) to another state $|0_N \Psi_{0_N}\rangle$ (where state N is unoccupied, $|0_N\rangle$), and the subsystem configuration of the remaining $(1, ..., N-1)$ electrons ($|\Psi_{1_N}\rangle$) is rotated into the configuration $|\Psi_{0_N}\rangle$. Taking cue from this decomposition, we can define the projection operator P_N using the η_N operator and its Hermitian conjugate

$$P_N = \mathcal{N}(1 + \eta_N + \eta_N^\dagger) \ . \tag{A.6}$$

Next, we solve for η_N by putting P_N (eq.(A.6)) into eq.(A.3), and projecting onto the state $|1_N, \Psi_{1_N}\rangle$

$$\hat{n}_N H \hat{n}_N |1_N, \Psi_{1_N}\rangle + \hat{n}_N H(1 - \hat{n}_N)\eta_N |1_N, \Psi_{1_N}\rangle = H'|1_N, \Psi_{1_N}\rangle \ , \tag{A.7}$$

$$(1 - \hat{n}_N)H(1 - \hat{n}_N)\eta_N |1_N, \Psi_{1_N}\rangle + (1 - \hat{n}_N)H \hat{n}_N |1_N, \Psi_{1_N}\rangle = H'\eta_N |1_N, \Psi_{1_N}\rangle \ , \tag{A.8}$$

$$\Rightarrow \eta_N = \frac{1}{H' - (1 - \hat{n}_N)H(1 - \hat{n}_N)}(1 - \hat{n}_N)H \hat{n}_N \ . \tag{A.9}$$

Given the symmetry properties of H' (eq.(A.4)), it supports the decomposition into a diagonal piece H'^D, and an off-diagonal piece H'^X_N constituting all electronic states apart from N

$$H' = H'^X_N + H'^D . \tag{A.10}$$

Using eq.(A.10), we can obtain a simple description of η_N

$$\eta_N = \frac{1}{\hat{\omega} - Tr_N(H^D(1 - \hat{n}_N))(1 - \hat{n}_N)}Tr_N(c^\dagger_N H)c_N , \tag{A.11}$$

where $\hat{\omega} = H'^D + H'^X_N - H^X_N$, and H^X_N has a definition similar to H'^X_N. $Tr_N(c^\dagger_N H)c_N$ is the collection of selected off-diagonal pieces of H involving the state N. Additionally, we note that a form for $\eta^\dagger_N$ can similarly be obtained by projecting onto state $|0_N, \Psi_{0_N}\rangle$

$$\eta^\dagger_N = \frac{1}{\hat{\omega} - Tr_N(H^D \hat{n}_N)\hat{n}_N}c^\dagger_N Tr_N(Hc_N) . \tag{A.12}$$

In the above equation $Tr_N(.)$ represents the partial tracing of the electronic state N, which is carried out in the electronic fock space. Putting $\eta_N$eq.(A.9) into eq.(A.7), and using the form for $\eta^\dagger_N$, we obtain the algebra for these operators

$$\{\eta^\dagger_N, \eta_N\} = 1 , \ [\eta^\dagger_N, \eta_N] = 2\hat{n}_N - 1 . \tag{A.13}$$

An additional set of relations for η_N and $\eta^\dagger_N$ are: $\eta^2_N = \eta^{\dagger 2} = 0$. The state $|\Psi\rangle$ can now be connected via a similarity transformation to the state $|1_N \Psi_{1_N}\rangle$

$$|\Psi\rangle = a_1 \exp(\eta_N)|1_N \Psi_{1_N}\rangle . \tag{A.14}$$

Note that in $|1_N \Psi_{1_N}\rangle$, the state N is now disentangled. Finally, we can construct the form for the unitary transformation U_N from the similarity transformation [99, 100]

$$U_N = \frac{1}{\sqrt{2}}(1 + \eta_N - \eta^\dagger_N) \tag{A.15}$$

Using the algebra eq(A.13) one can verify the identity $UU^\dagger = U^\dagger U = 1$.

B Derivation of the normal phase Hamiltonian in pseudospin subspace

A projection of the normal phase Hamiltonian eq.(2.4) in the charge pseudospin subspace gives the effective Hamiltonian for the normal metal phase of the 2D Hubbard model at 1/2-filling [44] as

$$H^* = \sum_{\substack{l=1, \\ i=(1,2)}}^{j} \epsilon_{\Lambda_l \hat{s}_i} A^z_{\Lambda_l \hat{s}_i} - \sum_{\substack{i,j, \\ k=1,2}} R^*_k A^z_{\Lambda_i, \hat{s}_k} A^z_{\Lambda_i, \hat{s}_k} . \tag{B.1}$$

The ground state of the gapless normal phase with 14 electrons in 28 states is then written as

$$|\Psi\rangle_{NP} = \prod_{i=0,n=(0,1)}^{6} |\downarrow_{i+21n}\rangle \prod_{i=7,n=(0,1)}^{13} |\uparrow_{i+7n}\rangle . \tag{B.2}$$

References

[1] P. Calabrese and J. Cardy, *Entanglement entropy and quantum field theory*, *Journal of Statistical Mechanics: Theory and Experiment* **2004** (2004) P06002.

[2] S. Ryu and T. Takayanagi, *Aspects of holographic entanglement entropy*, *Journal of High Energy Physics* **2006** (2006) 045.

[3] S. Ryu and T. Takayanagi, *Holographic derivation of entanglement entropy from the anti–de sitter space/conformal field theory correspondence*, *Physical review letters* **96** (2006) 181602.

[4] G. Vidal, *Entanglement renormalization*, *Physical review letters* **99** (2007) 220405.

[5] B. Swingle, *Entanglement entropy and the fermi surface*, *Physical review letters* **105** (2010) 050502.

[6] B. J. Brown, D. Loss, J. K. Pachos, C. N. Self and J. R. Wootton, *Quantum memories at finite temperature*, *Reviews of Modern Physics* **88** (2016) 045005.

[7] T. Nishioka, *Entanglement entropy: holography and renormalization group*, *Reviews of Modern Physics* **90** (2018) 035007.

[8] K. G. Wilson, *Renormalization group and critical phenomena. i. renormalization group and the kadanoff scaling picture*, *Physical review B* **4** (1971) 3174.

[9] K. G. Wilson, *Renormalization group and critical phenomena. ii. phase-space cell analysis of critical behavior*, *Physical Review B* **4** (1971) 3184.

[10] M. E. Fisher, *The renormalization group in the theory of critical behavior*, *Reviews of Modern Physics* **46** (1974) 597.

[11] V. Balasubramanian and P. Kraus, *Spacetime and the holographic renormalization group*, *Physical Review Letters* **83** (1999) 3605.

[12] J. De Boer, E. Verlinde and H. Verlinde, *On the holographic renormalization group*, *Journal of High Energy Physics* **2000** (2000) 003.

[13] I. Heemskerk, J. Penedones, J. Polchinski and J. Sully, *Holography from conformal field theory*, *Journal of High Energy Physics* **2009** (2009) 079.

[14] S.-S. Lee, *Holographic description of quantum field theory*, *Nuclear Physics B* **832** (2010) 567.

[15] H. Casini, M. Huerta and R. C. Myers, *Towards a derivation of holographic entanglement entropy*, *Journal of High Energy Physics* **2011** (2011) 36.

[16] I. Heemskerk and J. Polchinski, *Holographic and wilsonian renormalization groups*, *Journal of High Energy Physics* **2011** (2011) 31.

[17] S.-S. Lee, *Quantum renormalization group and holography*, *Journal of High Energy Physics* **2014** (2014) 76.

[18] M. Van Raamsdonk, *Building up spacetime with quantum entanglement*, *General Relativity and Gravitation* **42** (2010) 2323.

[19] G. Evenbly and G. Vidal, *Tensor network states and geometry*, *Journal of Statistical Physics* **145** (2011) 891.

[20] M. Nozaki, S. Ryu and T. Takayanagi, *Holographic geometry of entanglement renormalization in quantum field theories*, *Journal of High Energy Physics* **2012** (2012) 193.

[21] B. Swingle, *Entanglement renormalization and holography*, *Physical Review D* **86** (2012) 065007.

[22] B. Swingle, *Constructing holographic spacetimes using entanglement renormalization*, *arXiv preprint arXiv:1209.3304* (2012) .

[23] X.-L. Qi, *Exact holographic mapping and emergent space-time geometry*, *arXiv preprint arXiv:1309.6282* (2013) .

[24] C. H. Lee and X.-L. Qi, *Exact holographic mapping in free fermion systems*, *Physical Review B* **93** (2016) 035112.

[25] P. Hayden, S. Nezami, X.-L. Qi, N. Thomas, M. Walter and Z. Yang, *Holographic duality from random tensor networks*, *Journal of High Energy Physics* **2016** (2016) 9.

[26] M. Aguado and G. Vidal, *Entanglement renormalization and topological order*, *Physical review letters* **100** (2008) 070404.

[27] V. Giovannetti, S. Montangero and R. Fazio, *Quantum multiscale entanglement renormalization ansatz channels*, *Physical review letters* **101** (2008) 180503.

[28] R. N. Pfeifer, G. Evenbly and G. Vidal, *Entanglement renormalization, scale invariance, and quantum criticality*, *Physical Review A* **79** (2009) 040301.

[29] J. C. Bridgeman, A. O'Brien, S. D. Bartlett and A. C. Doherty, *Multiscale entanglement renormalization ansatz for spin chains with continuously varying criticality*, *Physical Review B* **91** (2015) 165129.

[30] B. Swingle and J. McGreevy, *Renormalization group constructions of topological quantum liquids and beyond*, *Physical Review B* **93** (2016) 045127.

[31] X. Wen, G. Y. Cho, P. L. Lopes, Y. Gu, X.-L. Qi and S. Ryu, *Holographic entanglement renormalization of topological insulators*, *Physical Review B* **94** (2016) 075124.

[32] Y. Gu, C. H. Lee, X. Wen, G. Y. Cho, S. Ryu and X.-L. Qi, *Holographic duality between (2+ 1)-dimensional quantum anomalous hall state and (3+ 1)-dimensional topological insulators*, *Physical Review B* **94** (2016) 125107.

[33] M. Gerster, M. Rizzi, P. Silvi, M. Dalmonte and S. Montangero, *Fractional quantum hall effect in the interacting hofstadter model via tensor networks*, *Physical Review B* **96** (2017) 195123.

[34] G. Vidal, *Class of quantum many-body states that can be efficiently simulated*, *Physical review letters* **101** (2008) 110501.

[35] G. Evenbly and G. Vidal, *Algorithms for entanglement renormalization*, *Physical Review B* **79** (2009) 144108.

[36] J. Haegeman, T. J. Osborne, H. Verschelde and F. Verstraete, *Entanglement renormalization for quantum fields in real space*, *Physical review letters* **110** (2013) 100402.

[37] Y.-Z. You, X.-L. Qi and C. Xu, *Entanglement holographic mapping of many-body localized system by spectrum bifurcation renormalization group*, *Physical Review B* **93** (2016) 104205.

[38] I. H. Kim and B. Swingle, *Robust entanglement renormalization on a noisy quantum computer*, *arXiv preprint arXiv:1711.07500* (2017) .

[39] K. Hyatt, J. R. Garrison and B. Bauer, *Extracting entanglement geometry from quantum states*, *Physical review letters* **119** (2017) 140502.

[40] R. Orús, *Tensor networks for complex quantum systems*, *Nature Reviews Physics* **1** (2019) 538.

[41] R. Orús, *A practical introduction to tensor networks: Matrix product states and projected entangled pair states*, *Annals of Physics* **349** (2014) 117.

[42] J. Biamonte and V. Bergholm, *Tensor networks in a nutshell*, *arXiv preprint arXiv:1708.00006* (2017) .

[43] S.-S. Lee, *Quantum renormalization group and holography*, *Journal of High Energy Physics* **2014** (2014) 76.

[44] A. Mukherjee and S. Lal, *Scaling theory for mott-hubbard transitions*, *arXiv preprint arXiv:1802.06528* (2018) .

[45] S. Pal, A. Mukherjee and S. Lal, *Correlated spin liquids in the quantum kagome antiferromagnet at finite field: a renormalization group analysis*, *New Journal of Physics* **21** (2019) 023019.

[46] P. Corboz and G. Vidal, *Fermionic multiscale entanglement renormalization ansatz*, *Physical Review B* **80** (2009) 165129.

[47] T. Barthel, C. Pineda and J. Eisert, *Contraction of fermionic operator circuits and the simulation of strongly correlated fermions*, *Physical Review A* **80** (2009) 042333.

[48] J. Haegeman, B. Swingle, M. Walter, J. Cotler, G. Evenbly and V. B. Scholz, *Rigorous free-fermion entanglement renormalization from wavelet theory*, *Physical Review X* **8** (2018) 011003.

[49] G. Evenbly and G. Vidal, *Entanglement renormalization in noninteracting fermionic systems*, *Physical Review B* **81** (2010) 235102.

[50] V. Murg, F. Verstraete, Ö. Legeza and R. M. Noack, *Simulating strongly correlated quantum systems with tree tensor networks*, *Physical Review B* **82** (2010) 205105.

[51] V. Balasubramanian, M. B. McDermott and M. Van Raamsdonk, *Momentum-space entanglement and renormalization in quantum field theory*, *Physical Review D* **86** (2012) 045014.

[52] X.-G. Wen, *Topological orders in rigid states*, *International Journal of Modern Physics B* **4** (1990) 239.

[53] J. LeBlanc, A. E. Antipov, F. Becca, I. W. Bulik, G. K.-L. Chan, C.-M. Chung et al., *Solutions of the two-dimensional hubbard model: benchmarks and results from a wide range of numerical algorithms*, *Physical Review X* **5** (2015) 041041.

[54] X.-G. Wen, *A systematic construction of gapped non-liquid states*, *arXiv preprint arXiv:2002.02433* (2020) .

[55] D. P. DiVincenzo, *Two-bit gates are universal for quantum computation*, *Physical Review A* **51** (1995) 1015.

[56] D. Gottesman, *The heisenberg representation of quantum computers*, *arXiv preprint quant-ph/9807006* (1998) .

[57] A. R. Brown and L. Susskind, *Second law of quantum complexity*, *Physical Review D* **97** (2018) 086015.

[58] C. Beny, *Causal structure of the entanglement renormalization ansatz*, *New Journal of Physics* **15** (2013) 023020.

[59] B. Swingle, *Entanglement entropy and the fermi surface*, *Physical review letters* **105** (2010) 050502.

[60] B. Swingle, *Conformal field theory approach to fermi liquids and other highly entangled states*, *Physical Review B* **86** (2012) 035116.

[61] M. M. Wolf, F. Verstraete, M. B. Hastings and J. I. Cirac, *Area laws in quantum systems: mutual information and correlations*, *Physical review letters* **100** (2008) 070502.

[62] S.-S. Lee, *Horizon as critical phenomenon*, *Journal of High Energy Physics* **2016** (2016) 44.

[63] D. Gottesman, *Stabilizer codes and quantum error correction*, *arXiv preprint quant-ph/9705052* (1997) .

[64] A. Almheiri, X. Dong and D. Harlow, *Bulk locality and quantum error correction in ads/cft*, *Journal of High Energy Physics* **2015** (2015) 163.

[65] F. Pastawski, B. Yoshida, D. Harlow and J. Preskill, *Holographic quantum error-correcting codes: Toy models for the bulk/boundary correspondence*, *Journal of High Energy Physics* **2015** (2015) 149.

[66] I. H. Kim and M. J. Kastoryano, *Entanglement renormalization, quantum error correction, and bulk causality*, *Journal of High Energy Physics* **2017** (2017) 40.

[67] A. J. Ferris and D. Poulin, *Tensor networks and quantum error correction*, *Physical review letters* **113** (2014) 030501.

[68] A. Y. Kitaev, *Fault-tolerant quantum computation by anyons*, *Annals of Physics* **303** (2003) 2.

[69] H. Bombin and M. Martin-Delgado, *Topological quantum error correction with optimal encoding rate*, *Physical Review A* **73** (2006) 062303.

[70] H. Bombin, R. S. Andrist, M. Ohzeki, H. G. Katzgraber and M. A. Martín-Delgado, *Strong resilience of topological codes to depolarization*, *Physical Review X* **2** (2012) 021004.

[71] I. H. Kim, *Noise-resilient preparation of quantum many-body ground states*, *arXiv preprint arXiv:1703.00032* (2017) .

[72] R. Salakhutdinov and G. Hinton, *Deep boltzmann machines*, in *Artificial intelligence and statistics*, pp. 448–455, 2009.

[73] L. P. Kadanoff, *Statistical physics: statics, dynamics and renormalization*. World Scientific Publishing Company, 2000.

[74] L. P. Kadanoff, A. Houghton and M. C. Yalabik, *Variational approximations for renormalization group transformations*, *Journal of Statistical Physics* **14** (1976) 171.

[75] P. Mehta and D. J. Schwab, *An exact mapping between the variational renormalization group and deep learning*, *arXiv preprint arXiv:1410.3831* (2014) .

[76] N. Tishby and N. Zaslavsky, *Deep learning and the information bottleneck principle*, in *2015 IEEE Information Theory Workshop (ITW)*, pp. 1–5, IEEE, 2015.

[77] X. Gao and L.-M. Duan, *Efficient representation of quantum many-body states with deep neural networks*, *Nature communications* **8** (2017) 1.

[78] S. Lu, X. Gao and L.-M. Duan, *Efficient representation of topologically ordered states with restricted boltzmann machines*, *Physical Review B* **99** (2019) 155136.

[79] D. Liu, S.-J. Ran, P. Wittek, C. Peng, R. B. García, G. Su et al., *Machine learning by unitary tensor network of hierarchical tree structure*, New Journal of Physics **21** (2019) 073059.

[80] C. Bény, *Deep learning and the renormalization group*, arXiv preprint arXiv:1301.3124 (2013) .

[81] Y.-Z. You, Z. Yang and X.-L. Qi, *Machine learning spatial geometry from entanglement features*, Physical Review B **97** (2018) 045153.

[82] H.-Y. Hu, S.-H. Li, L. Wang and Y.-Z. You, *Machine learning holographic mapping by neural network renormalization group*, arXiv preprint arXiv:1903.00804 (2019) .

[83] N. Cohen, O. Sharir and A. Shashua, *On the expressive power of deep learning: A tensor analysis*, in *Conference on Learning Theory*, pp. 698–728, 2016.

[84] Y. Levine, O. Sharir, N. Cohen and A. Shashua, *Quantum entanglement in deep learning architectures*, Physical review letters **122** (2019) 065301.

[85] S.-H. Li and L. Wang, *Neural network renormalization group*, Physical review letters **121** (2018) 260601.

[86] K. Hashimoto, S. Sugishita, A. Tanaka and A. Tomiya, *Deep learning and the ads/cft correspondence*, Physical Review D **98** (2018) 046019.

[87] A. Mukherjee and S. Lal, *Scaling theory for mott-hubbard transitions- i :t = 0 phase diagram of the 1/2-filled hubbard model*, under review (2019) .

[88] M. Oshikawa and T. Senthil, *Fractionalization, topological order, and quasiparticle statistics*, Physical review letters **96** (2006) 060601.

[89] X. Chen, Z.-C. Gu and X.-G. Wen, *Local unitary transformation, long-range quantum entanglement, wave function renormalization, and topological order*, Physical review b **82** (2010) 155138.

[90] S. Pal, A. Mukherjee and S. Lal, *Topological approach to quantum liquid ground states on geometrically frustrated heisenberg antiferromagnets*, Journal of Physics: Condensed Matter **32** (2020) 165805.

[91] S. Pal and S. Lal, *Magnetization plateaus of the quantum pyrochlore heisenberg antiferromagnet*, Physical Review B **100** (2019) 104421.

[92] A. Mukherjee and S. Lal, *Scaling theory for mott-hubbard transitions- ii : Quantum criticality of the doped mott insulator*, under review (2019) .

[93] Y.-Z. You, X.-L. Qi and C. Xu, *Entanglement holographic mapping of many-body localized system by spectrum bifurcation renormalization group*, Physical Review B **93** (2016) 104205.

[94] X.-G. Wen, *Topological orders in rigid states*, International Journal of Modern Physics B **4** (1990) 239.

[95] S. A. Kivelson, D. S. Rokhsar and J. P. Sethna, *Topology of the resonating valence-bond state: Solitons and high-t c superconductivity*, Physical Review B **35** (1987) 8865.

[96] N. Laflorencie, *Quantum entanglement in condensed matter systems*, Physics Reports **646** (2016) 1.

[97] R. Shwartz-Ziv and N. Tishby, *Opening the black box of deep neural networks via information*, arXiv preprint arXiv:1703.00810 (2017) .

[98] T. Parr and J. Howard, *The matrix calculus you need for deep learning*, arXiv preprint arXiv:1802.01528 (2018) .

[99] K. Suzuki, *Construction of hermitian effective interaction in nuclei: General relation between hermitian and non-hermitian forms*, Progress of Theoretical Physics **68** (1982) 246.

[100] I. Shavitt and L. T. Redmon, *Quasidegenerate perturbation theories. a canonical van vleck formalism and its relationship to other approaches*, The Journal of Chemical Physics **73** (1980) 5711.